Development and Implementation of a New Computational Strategy for the Prediction of Elastoplastic Buckling

M. BelHadjAmor [*,†], M. Ben Bettaieb [‡,§,¶], S. Mezlini [*] and F. Abed-Meraim [‡,§]

[*]*Laboratoire de Génie Mécanique*
Ecole Nationale d'Ingénieurs de Monastir
Université de Monastir, 5019 Monastir, Tunisie

[†]*Ecole Nationale d'Ingénieurs de Carthage*
Université de Carthage, 2035 Tunis, Tunisie

[‡]*Université de Lorraine, CNRS,*
Arts et Métiers Institute of Technology
LEM3 F-57070 Metz, France

[§]*DAMAS, Laboratory of Excellence on Design*
of Alloy Metals for low-mAss Structures
Université de Lorraine, France
[¶]*Mohamed.BenBettaieb@ensam.eu*

This study proposes an innovative computational strategy to predict the initiation of elastoplastic buckling in shell structures. This strategy is developed in connection with ABAQUS/Standard Finite Element (FE) code. Toward this objective, two constitutive frameworks are implemented as User MATerial subroutines (UMATs) into this FE code; namely, the incremental flow theory of plasticity and the total deformation theory. These frameworks are formulated under the plane-stress condition, which is particularly suitable for modeling sheet structures and which enhances computational efficiency. Elastoplastic buckling is detected by the Hill loss of uniqueness criterion, which establishes that buckling occurs when the global stiffness matrix, derived from the finite element computations, becomes singular. To determine this matrix and investigate its singularity, a Python script is developed and combined to the ABAQUS computations. The reliability and accuracy of this computational strategy are assessed through various representative numerical examples. The effect of some geometric and material parameters on the onset of elastoplastic buckling in both thin and thick plates, as well as cruciform columns, is investigated and compared to reference results from the literature. The findings of the present contribution can serve as useful reference guidelines for ABAQUS/Standard users, offering valuable insights for predicting the occurrence of elastoplastic buckling,

[¶]Corresponding author.

even in metallic structures characterized by complex mechanical behavior and geometric configurations.

Keywords: Structural instability; elastoplastic buckling; Hill's loss of uniqueness criterion; deformation theory; flow theory; finite element analysis.

1. Introduction

The elastoplastic buckling of shell structures has attracted significant interest from both industrial and academic communities. Therefore, it is crucial to develop suitable tools and techniques capable of reliably predicting critical buckling loads and the associated modes. Consequently, several analytical and numerical techniques have been designed in the literature to achieve such predictions. Analytical approaches allow simplified yet insightful predictions of elastoplastic buckling in some basic configurations (with perfect geometric structures and simple boundary conditions). The foundational works in this realm have been initiated by Shanley [1947], who pioneered an analytical approach based on the well-known tangent modulus theory. Notable contributions in this area include the work of Bleich [1952], who developed a unified framework to determine the elastoplastic buckling behavior of simply supported square plates subjected to uniaxial compression. The extension of Bleich's framework to encompass the elastoplastic buckling of rectangular plates under alternative boundary conditions has been undertaken in other publications, such as Wang *et al.* [2001]. Additionally, in-depth analytical examinations of elastoplastic buckling phenomena in both simple and cruciform columns under diverse boundary conditions have been presented by various authors [Cicala, 1950; Hutchinson and Budiansky, 1976; Onat and Drucker, 1953], employing the deformation and flow theories of plasticity to characterize the sheet mechanical behavior. However, real-world applications generally involve complex geometries and boundary conditions that surpass the scope of the aforementioned configurations. Furthermore, analytical models use simplified constitutive frameworks, which are sometimes inadequate to accurately model the mechanical behavior of actual structures, as several relevant physical phenomena are not considered, such as kinematic and distortional hardening, elastic and plastic anisotropy, damage and non-associativity of the flow rule. Consequently, analytical approaches are not able to address elastoplastic buckling in such applications. In response, numerical approaches have been widely used due to their ability to predict elastoplastic buckling in complex structures by employing advanced constitutive frameworks. Among the numerical approaches, three prominent numerical strategies stand out: the Ritz method, the Differential Quadrature Method (DQM) and the classical Finite Element Method (FEM). The Ritz method approximates the displacements of the structure under consideration using trial functions that adhere to geometric boundary conditions and anticipated mode shapes. This method has been employed in several contributions [Smith *et al.*, 2003; Wang and Aung, 2007] to predict the onset of elastoplastic buckling in thin and thick plates under different loading conditions. The Ritz method

validity, convergence and accuracy have been successfully demonstrated across a spectrum of plate shapes (such as rectangular, triangular and elliptical shapes) subjected to different boundary conditions, including simply supported plates and fixed/supported plates. The DQM involves discretizing the governing differential equations, such as the equilibrium and plasticity constitutive equations, into a system of algebraic equations through the application of numerical differentiation with quadrature weights and nodes. Solving this transformed algebraic system allows predicting the critical buckling stresses and the corresponding mode shapes. The DQM has been applied by Shamass *et al.* [2017], Wang and Huang [2009] and Zhang and Wang [2011] to predict the occurrence of elastoplastic buckling in cylinders as well as in thin and thick rectangular plates subjected to biaxial loading. The FEM has also been extensively used to predict the incipience of elastoplastic buckling by following either a bifurcation buckling method or a limit-point buckling method. In this field, elastic buckling is predicted via ABAQUS/Standard '*Buckle*' module, which is a bifurcation method that relies on a linear perturbation analysis. Under this approach, the behavior of the structure is analyzed around an initial equilibrium state and small perturbations are applied to the structure. The goal of this approach is to identify the bifurcation point by computing the critical load multiplier at which the structure becomes unstable, indicating the factor by which the applied loads must be multiplied to cause buckling. The '*Buckle*' module is limited, however, to the prediction of elastic buckling due to its underlying linearity assumption. To estimate the onset of elastoplastic buckling by ABAQUS finite element code, the limit-point method has commonly been used [Wagner *et al.*, 2019; Ning and Pellegrino, 2017]. This approach identifies the limit-point buckling by introducing initial imperfections, such as geometric irregularities or residual stresses, that will lead to the buckled shape of the studied structure. The motivation of introducing such initial imperfections is to induce some local weakening in the investigated structure, which then contributes to trigger the overall structural instability. In this approach, the Riks method (also known as the arc-length method) is used to control the applied loading. The critical buckling load is determined when the applied force reaches its maximum value, called the limit point. This approach reveals high sensitivity of the predicted buckling load to the initial imperfection magnitude, particularly in the elastoplastic deformation domain. However, in practice, some structures (mainly thin components) are prone to bifurcation phenomena that may occur prior to limit-point buckling [Hopperstad *et al.*, 1999]. In such circumstances, it seems relevant to extend the application of the bifurcation buckling method to non-linear materials and structures. For this purpose, the Hill instability criterion [Hill, 1958] has been incorporated into several finite element software tools to evaluate the bifurcation buckling of non-linear structures. This theory can be viewed as a generalization of the tangent modulus approach to the case of general three-dimensional elastoplastic structures. It establishes that elastoplastic buckling occurs when the solution to the boundary value problem becomes non-unique, indicating the existence of at least two velocity fields, and the associated stress rate tensors,

as solutions to the governing equations. From a computational perspective, this criterion amounts to the singularity of the global stiffness matrix derived from the finite element computations. A number of researchers have developed their in-house finite element code to predict the onset of elastoplastic buckling on the basis of the Hill criterion for usual structures, such as thin plates or tubes [Legendre *et al.*, 2019; Do *et al.*, 2023]. Despite their interest, in-house codes confront several limitations that hinder their application in industrial contexts, including the lack of documentation and user support, the limited computational efficiency, and potential incompatibility with other software tools. Therefore, the Hill loss of uniqueness criterion has been implemented in several industrial finite element codes, such as Aster [Combescure and Jullien, 2015] and Cast3M [Jacquet *et al.*, 2022], enabling the prediction of elastoplastic buckling in complex geometries with non-linear constitutive frameworks. It is worth noting, however that, for the commercial version of the ABAQUS Software package, the Hill criterion is implemented solely for elastic buckling analysis. Consequently, the current contribution seeks to bridge this gap by implementing a computational strategy into ABAQUS finite element code, based on the Hill criterion, for the prediction of elastoplastic buckling in perfect shell structures (i.e., without having to recourse to initial imperfections). Our method can be used in complementarity with the Riks method to model the two types of buckling, namely bifurcation and limit-point instabilities, in problems involving geometric and material non-linearities. This strategy is based on the following tasks:

(i) The implementation of an elastoplastic constitutive framework in the form of a User MATerial subroutine (UMAT). As explained in Zhu *et al.* [2022], when ABAQUS/Standard built-in mechanical modeling is used, the global stiffness matrix is constructed only on the basis of the elastic contribution. Hence, the use of a UMAT is essential to take the plastic behavior into account in the stiffness matrix. In this contribution, both the deformation theory and flow theory of plasticity are employed to model the mechanical behavior.
(ii) The development of a Python script in order to connect the finite element computations with the Hill bifurcation criterion, thus enabling elastoplastic buckling analyses. This script, executed as post-processing of finite element computations, allows assembling the global stiffness matrix from elementary matrices, computing the eigenvalues and eigenvectors of this matrix, and determining the critical buckling stress and corresponding mode shape.

The accuracy and reliability of this numerical strategy are thoroughly assessed through a set of various and representative numerical examples, including the buckling analysis of both thin and thick plates as well as cruciform columns. Consequently, this paper stands as a valuable reference for ABAQUS/Standard users seeking to predict elastoplastic buckling involving metallic structures characterized by complex mechanical behavior and geometric shapes. The choice of ABAQUS/Standard code is motivated by our objective of widely disseminating

our findings, considering that this software package represents one of the most widely adopted finite element programs within both academic and industrial communities. This large dissemination would facilitate broader outreach to the research community. The subsequent sections are structured as follows:

- Section 2 provides a comprehensive overview of the theoretical formulation and numerical implementation of the elastoplastic buckling criterion.
- Section 3 is devoted to the presentation of the constitutive frameworks used to model the mechanical behavior and the numerical aspects relating to their implementation in ABAQUS/Standard code.
- The validation of our numerical strategy is rigorously conducted in Sec. 4 by comparing its results to those presented in existing literature. The results of this section demonstrate the reliability and accuracy of the proposed strategy.

2. Elastoplastic Buckling Criterion

2.1. *Theoretical formulation*

Plastic buckling represents a structural instability phenomenon wherein a slender component, subjected to compressive loading undergoes sudden and substantial deflection, potentially leading to failure. To predict elastoplastic buckling, the Hill non-uniqueness criterion [Hill, 1958] is employed. This bifurcation theory provides a methodology for computing the critical buckling stresses and the associated buckling modes. As a foundation for presenting the Hill loss of uniqueness criterion, we begin with introducing the relevant form of virtual power principle, as established in Zhu *et al.* [2022]:

$$\int_{\mathcal{V}_0} [\delta\mathbf{d} : \mathring{\boldsymbol{\tau}} - 2\boldsymbol{\tau} : (\mathbf{d} \cdot \delta\mathbf{d}) + \boldsymbol{\tau} : (\mathbf{l}^T \cdot \delta\mathbf{l})] d\mathcal{V}_0 = \int_{\mathcal{S}_0} \delta\mathbf{v} \cdot \dot{\mathbf{t}}_0 \, \mathrm{d}\mathcal{S}_0 + \int_{\mathcal{V}_0} \delta\mathbf{v} \cdot \dot{\mathbf{b}}_0 \, \mathrm{d}\mathcal{V}_0, \tag{1}$$

where:

- $\mathbf{v}$ is the velocity field.
- $\mathcal{V}_0$ is the volume of the reference configuration and $\mathcal{S}_0$ its boundary surface.
- $\mathbf{l}$ is the velocity gradient, defined as $\partial\mathbf{v}/\partial\mathbf{x}$, and $\delta\mathbf{l}$ its virtual counterpart.
- $\mathbf{d}$ is the strain rate, defined as the symmetric part of $\mathbf{l}$ and $\delta\mathbf{d}$ its virtual counterpart.
- $\mathring{\tau}$ is the Jaumann rate of the Kirchhoff stress $\boldsymbol{\tau}$.
- $\dot{\mathbf{t}}_0$ denotes the nominal traction rate prescribed on $\mathcal{S}_0$.
- $\dot{\mathbf{b}}_0$ refers to the body force rate per unit volume in the reference configuration.
- $\delta\mathbf{v}$ is the virtual counterpart of the velocity field $\mathbf{v}$.
- $\bullet \cdot \bullet$ refers to the simple contraction or contraction on one index.
- $\bullet : \bullet$ denotes the double contraction or contraction on two indices.

The expression provided in Eq. (1) is similar to the virtual power principle formulation used in ABAQUS FE code. As corroborated by studies [Hutchinson, 1972; Nguyen, 2000], the initiation of elastoplastic buckling occurs when the following equality holds:

$$\int_{\mathcal{V}_0} \left[\delta\mathbf{d} : \mathring{\boldsymbol{\tau}} - 2\boldsymbol{\tau} : (\mathbf{d}\cdot\delta\mathbf{d}) + \boldsymbol{\tau} : \left(\mathbf{l}^T\cdot\delta\mathbf{l}\right)\right] d\mathcal{V}_0 = 0. \tag{2}$$

On the other hand, the Jaumann rate of the Kirchhoff stress $\mathring{\boldsymbol{\tau}}$ is related to the strain rate $\mathbf{d}$ through the modulus $\hat{\mathbb{C}}^{\text{ep}}$ as follows:

$$\mathring{\boldsymbol{\tau}} = \hat{\mathbb{C}}^{\text{ep}} : \mathbf{d}. \tag{3}$$

In the constitutive equations used in ABAQUS FE code in the form of built-in material models or implemented as user-defined material subroutines (UMATs), the Cauchy stress tensor $\boldsymbol{\sigma}$ is usually adopted to measure the stress state. To relate the Jaumann rate of the Cauchy stress $\mathring{\boldsymbol{\sigma}}$ to the strain rate $\mathbf{d}$, let us introduce the elastoplastic tangent modulus $\mathbb{C}^{\text{ep}}$, such that

$$\mathring{\boldsymbol{\sigma}} = \mathbb{C}^{\text{ep}} : \mathbf{d}. \tag{4}$$

By following an updated Lagrangian formulation, we can easily deduce the following relation between moduli $\hat{\mathbb{C}}^{\text{ep}}$ and $\mathbb{C}^{\text{ep}}$ [Akpama *et al.*, 2017]:

$$\mathbb{C}^{\text{ep}} = \hat{\mathbb{C}}^{\text{ep}} - \boldsymbol{\sigma}\otimes\mathbf{I}_2, \tag{5}$$

where $\mathbf{I}_2$ is the second-order identity tensor $\bullet\otimes\bullet$ denotes the tensor product. The analytical expressions of modulus $\mathbb{C}^{\text{ep}}$ corresponding to the used constitutive frameworks (namely, the flow and the total deformation theories) will be provided in Secs. 3.2.1 and 3.2.2, respectively.

Using finite element discretization, we can derive the velocity field $\mathbf{v}$ and the strain rate $\mathbf{d}$ from the nodal displacement rate vector $\dot{\mathbf{q}}$ through the interpolation rule:

$$\mathbf{v} = \mathbf{N}\cdot\dot{\mathbf{q}}; \quad \mathbf{d} = \frac{1}{2}\left(\mathbf{B}+\mathbf{B}^T\right)\cdot\dot{\mathbf{q}} \tag{6}$$

with $\mathbf{N}$ standing for the shape function vector, and $\mathbf{B}$ its derivative with respect to the spatial coordinates $\mathbf{x}$. Substituting Eqs. (3) and (6) into the different components of Eq. (1) yields the following expressions:

$$\begin{cases} \displaystyle\int_{\mathcal{V}_0}[\delta\mathbf{d} : \tilde{\boldsymbol{\tau}}]d\mathcal{V}_0 = \int_{\mathcal{V}_0}[\delta\mathbf{d} : \hat{\mathbb{C}}^{\text{ep}} : \mathbf{d}]d\mathcal{V}_0 = \delta\dot{\mathbf{q}}^T\cdot\left[\int_{\mathcal{V}_0}\mathbf{B}^T\cdot\hat{\mathbb{C}}^{\text{ep}}\cdot\mathbf{B}\,d\mathcal{V}_0\right] \\ \qquad\qquad \cdot\dot{\mathbf{q}} = \delta\dot{\mathbf{q}}^T\cdot\mathbf{K}_M\cdot\dot{\mathbf{q}}, \\ \displaystyle\int_{\mathcal{V}_0}\left[-2\boldsymbol{\tau} : (\mathbf{d}\cdot\delta\mathbf{d}) + \boldsymbol{\tau} : \left(\mathbf{l}^T\cdot\delta\mathbf{l}\right)\right] d\mathcal{V}_0 = \delta\dot{\mathbf{q}}^T\cdot\mathbf{K}_{\text{GNL}}\cdot\dot{\mathbf{q}}, \\ \displaystyle\int_{\mathcal{S}_0}\delta\mathbf{v}\cdot\dot{\mathbf{t}}_0\ \mathrm{d}\mathcal{S}_0 + \int_{\mathcal{V}_0}\delta\mathbf{v}\cdot\dot{\mathbf{b}}_0\ \mathrm{d}\mathcal{V}_0 = \delta\dot{\mathbf{q}}^T\cdot\dot{\mathbf{r}}, \end{cases} \tag{7}$$

where:

- $\mathbf{K}_M$ represents the portion of the global stiffness matrix corresponding to the mechanical behavior of the structure.
- $\mathbf{K}_{\text{GNL}}$ represents the contribution to the global stiffness matrix that arises from geometric non-linearities.
- $\dot{\mathbf{r}}$ is the residual vector rate.

Then, Eq. (1) can be expressed in the following discretized matrix form:

$$[\mathbf{K}_M + \mathbf{K}_{\text{GNL}}] \cdot \dot{\mathbf{q}} = \mathbf{K} \cdot \dot{\mathbf{q}} = \dot{\mathbf{r}}. \tag{8}$$

At an early deformation stage from the beginning of loading, all the eigenvalues of the stiffness matrix $\mathbf{K}$ are positive indicating a stable and unique solution for Eq. (8). However, as the loading proceeds, there comes a point where the stiffness matrix $\mathbf{K}$ becomes singular. At this time, the solution of Eq. (8) becomes non-unique, which signals the occurrence of elastic or elastoplastic buckling by the condition:

$$\det[\mathbf{K}] = 0. \tag{9}$$

2.2. *Numerical implementation*

The Hill loss of uniqueness criterion expressed by Eq. (9) is implemented in a Python script that serves as a post-processing tool for the finite element computations. Python has been deliberately chosen as scripting language due to its numerous benefits in extracting critical information from an ABAQUS database. The selection of Python is further justified by its incorporation of high-performance libraries, including NumPy and SciPy. The decision to opt for Python is additionally motivated by exploiting these libraries. These libraries provide a robust N-dimensional array structure alongside essential linear algebra techniques, thereby facilitating efficient matrix computations. The benefits are two-fold: a notable reduction in computation time and judicious employment of memory resources. Consequently, the Python language emerges as an astute and pragmatic choice for constructing this pivotal component of the proposed computational strategy. The operational sequence of this script is succinctly delineated in the following summary box.

Box 1. Key steps for the implementation of the Hill loss of uniqueness criterion.

The main steps for the implementation of the elastoplastic buckling analysis are summarized as follows:

- **Step 1:** Prepare the ABAQUS input file by considering the following tasks (Appendix B):
  - Add an independent step, right after the initial step, to extract the initial global stiffness matrix $\mathbf{K}_{\text{INIT}}$ assembled by ABAQUS code with

the applied boundary conditions (those illustrated in Fig. 3(a)for the plates). The constrained degrees of freedom appear in the stiffness matrix $\mathbf{K}_{\text{INIT}}$ with very large components ($1e^{+36}$).
- Call one of the two user subroutines UMAT (the deformation theory or the flow theory) with the corresponding material parameters.
- Activate the option '*nlgeom*' in the '*Step*' section. This activation is essential to take into account the contribution of the geometric non-linearities $\mathbf{K}_{\text{GNL}}$ (see Eq. (8)) in the global stiffness matrix $\mathbf{K}$.
- Add the following option required to output the elementary stiffness matrices $\mathbf{K}_{el}$ at the end of the '*Step*' section:
  *Element Matrix Output, Elset = Set-1, File Name = myMatrix, Frequency = n, Output File = User Defined, Stiffness = Yes
  In the previous command, n is the record frequency. In all of our FE simulations, we have set n to 1. Hence, the elementary stiffness matrices are stored at the end of each FE increment.

- **Step 2:** Run the finite element simulation. The elementary stiffness matrices $\mathbf{K}_{el}$ will be saved in an external file with the extension '.mtx'. This file will contain the necessary stiffness data required for the elastoplastic buckling analysis.

- **Step 3:** Run the developed Python code to manage the main following tasks for each recorded time (Appendix C):
  - Assemble the elementary stiffness matrices stored in the '.mtx' file by using the connectivity of the different nodes of the finite elements to determine the global stiffness matrix $\mathbf{K}$.
  - Prescribe the initial boundary conditions (before applying the buckling load): Eliminate the constrained degrees of freedom to obtain a reduced form of matrix $\mathbf{K}$ (designated hereafter as $\tilde{\mathbf{K}}$). To identify the constrained degrees of freedom, the Python code extracts the subscripts of constrained components from $\mathbf{K}_{\text{INIT}}$.
  - Compute the eigenvalues and eigenvectors of matrix $\tilde{\mathbf{K}}$. The completion of this task entails high CPU and memory costs. To efficiently optimize this task, the eigenvalue and eigenvector computation are performed by using the functions 'linalg.eigsh' and 'linalg.inv' of the NumPy library.
  - Extract the buckling load from the '.odb' file by summing the reaction forces applied on the boundary of the finite element mesh at each recorded time. The buckling stress is obtained by dividing the sum of reaction forces by the plate section.

3. Constitutive Frameworks

3.1. *Theoretical formulation*

In this investigation, two constitutive frameworks are employed to describe the elastoplastic behavior of the studied metal structures: the classical flow theory (FT), also known as the incremental theory of plasticity and the total deformation (Henkey) theory (DT). When dealing with elastoplastic buckling, which often occurs within the finite strain and large displacement range, it becomes essential to adopt a finite strain formulation for both constitutive models. The equations corresponding to both frameworks are implemented into ABAQUS in the form of UMAT subroutines. In line with typical implementations of inelastic models in ABAQUS, the constitutive equations are formulated in a co-rotational frame; that is to say, using rotation-compensated variables [Hughes and Winget, 1980]. Consequently, the Jaumann rate $\mathring{\mathbf{T}}$ of a second-order tensor $\mathbf{T}$ becomes identical to its simple time derivative $\dot{\mathbf{T}}$, with $\mathbf{T}$ being expressed in an appropriate co-rotational frame. Hence, the constitutive equations presented in Secs. 3.1.1 and 3.1.2 will involve simple time derivatives, making them identical in form to those of a small strain formulation. This numerical strategy enables efficient and accurate computations. Additionally, the two constitutive frameworks are formulated under the plane-stress condition, which is more suitable for modeling shell structure buckling and which increases the computational efficiency, as compared to the classical 3D formulation. In fact, as has been clearly shown in Bathe [2014], the plane-stress assumption results in significant savings in memory, storage space and computational time. Therefore, all the constitutive equations will be formulated in a compact matrix form, under the plane-stress condition, to ensure efficiency of the numerical implementation. In particular, the strain and stress tensors and their derivatives will be stored in the following vector forms (without modification of the notations):

$$\boldsymbol{\varepsilon} = \{\varepsilon_{11}, \varepsilon_{22}, 2\varepsilon_{12}\}^T ; \quad \boldsymbol{\sigma} = \{\sigma_{11}, \sigma_{22}, \sigma_{12}\}^T . \tag{10}$$

Furthermore, a fourth-order tensor $\mathbb{T}$ will be stored in the following matrix form:

$$\mathbb{T} = \begin{bmatrix} T_{1111} & T_{1122} & T_{1112} \\ T_{2211} & T_{2222} & T_{2212} \\ T_{1211} & T_{1222} & T_{1212} \end{bmatrix} . \tag{11}$$

Consequently, the double contraction product $\mathbb{T} : \mathbf{T}$ between a fourth-order tensor $\mathbb{T}$ and a second-order tensor $\mathbf{T}$ will be replaced by the simple matrix product $\mathbb{T} \cdot \mathbf{T}$ between the matrix form of $\mathbb{T}$ and the vector form of $\mathbf{T}$.

3.1.1. *Elastoplastic flow theory of plasticity*

In this constitutive modeling, all of the governing equations are formulated in a rate form to accurately capture the material behavior. The total in-plane strain rate $\mathbf{d}$

is additively decomposed into its elastic and plastic parts, denoted as $\mathbf{d}^e$ and $\mathbf{d}^p$, respectively:

$$\mathbf{d} = \mathbf{d}^e + \mathbf{d}^p \quad \text{with } \mathbf{d} = \{d_{11}, d_{22}, 2d_{12}\}^T. \tag{12}$$

Under the plane-stress condition, the elastic strain rate $\mathbf{d}^e$ is defined by the hypo-elastic law:

$$\mathbf{d}^e = \mathbb{S}^e \cdot \dot{\boldsymbol{\sigma}}, \tag{13}$$

where:

- $\mathbb{S}^e$ is the in-plane elastic compliance matrix, defined in terms of the Poisson ratio ν and the Young modulus E as follows:

$$\mathbb{S}^e = \frac{1}{E}\begin{bmatrix} 1 & -\nu & 0 \\ -\nu & 1 & 0 \\ 0 & 0 & 2(1+\nu) \end{bmatrix}. \tag{14}$$

- $\dot{\boldsymbol{\sigma}}$ is the rate of the in-plane Cauchy stress, stored in a vector form as $\{\dot{\sigma}_{11}, \dot{\sigma}_{22}, \dot{\sigma}_{12}\}^T$.

Plasticity is assumed to follow an associated flow rule. Hence, the plastic strain rate $\mathbf{d}^p$ is defined by the normality law establishing the relationship between $\mathbf{d}^p$ and the stress tensor $\boldsymbol{\sigma}$ during plastic deformation:

$$\mathbf{d}^p = d^p_{\text{eq}} \frac{\mathbb{I}_d \cdot \boldsymbol{\sigma}}{\sigma_{\text{eq}}}, \tag{15}$$

where $\mathbb{I}_d$ is a 3×3 matrix allowing the stress state to be projected in the deviator space:

$$\mathbb{I}_d = \begin{bmatrix} 1 & -1/2 & 0 \\ -1/2 & 1 & 0 \\ 0 & 0 & 3 \end{bmatrix}. \tag{16}$$

As to σ_{eq} and d^p_{eq}, they represent the von Mises equivalent stress and the equivalent plastic strain rate, respectively, defined as

$$\begin{aligned} \sigma_{\text{eq}} &= \sqrt{\boldsymbol{\sigma}^T \cdot \mathbb{I}_d \cdot \boldsymbol{\sigma}} = \sqrt{(\sigma_{11})^2 + (\sigma_{22})^2 - (\sigma_{11}\sigma_{22}) + 3\,(\sigma_{12})^2}, \\ d^p_{\text{eq}} &= \sqrt{\mathbf{d}^{pT} \cdot \mathbb{I}_d^{-1} \cdot \mathbf{d}^p} = \sqrt{(4/3)\left[(d^p_{11})^2 + (d^p_{12})^2 + (d^p_{22})^2 + (d^p_{11}d^p_{22})\right]}. \end{aligned} \tag{17}$$

The plastic flow is given by the consistency condition:

$$f(\boldsymbol{\sigma}, \sigma_Y) = \sigma_{\text{eq}} - \sigma_Y \leq 0; \quad d^p_{\text{eq}} \geq 0, \tag{18}$$

where:

- f is the yield function.

- σ_Y is the yield stress defined by the Ramberg–Osgood relationship [Ramberg and Osgood, 1943]:

$$\varepsilon^p_{\text{eq}} = \frac{K\sigma_0}{E}\left(\frac{\sigma_Y}{\sigma_0}\right)^c \Leftrightarrow \sigma_Y = \sigma_0\left(\frac{E\varepsilon^p_{\text{eq}}}{K\sigma_0}\right)^{1/c}, \tag{19}$$

with $\varepsilon^p_{\text{eq}}$ the equivalent plastic strain equal to $\int_0^t d^p_{\text{eq}}dt$, σ_0 the nominal yield strength (also called 'proof stress'), K the yield offset and c a hardening exponent. The Ramberg–Osgood hardening law has been chosen due to its well-established capability of accurately modeling the non-linear stress–strain behavior of materials undergoing two-stage strain hardening. Additionally, the Ramberg–Osgood law is widely used in the literature, particularly for modeling plastic buckling, which facilitates comparison with other studies and enhances the robustness of our findings. Specifically, the analytical model developed in Wang *et al.* [2001], used to validate our numerical strategy, was built using the Ramberg–Osgood hardening law. Furthermore, the use of this hardening model ensures that plasticity is accounted for from the beginning of the loading, thereby ensuring that buckling occurs within the plastic range.

The combination of Eqs. (12), (13) and (15) leads to the following relationship between the stress and strain rates (the Prandtl–Reuss equation):

$$\mathbf{d} = \mathbb{S}^e \cdot \dot{\boldsymbol{\sigma}} + d^p_{\text{eq}}\frac{\mathbb{I}_d \cdot \boldsymbol{\sigma}}{\sigma_{\text{eq}}}. \tag{20}$$

3.1.2. *Total deformation theory*

For the total deformation theory, the total strain $\boldsymbol{\varepsilon}$ is additively decomposed into its elastic and plastic components, $\boldsymbol{\varepsilon}^e$ and $\boldsymbol{\varepsilon}^p$, respectively:

$$\boldsymbol{\varepsilon} = \boldsymbol{\varepsilon}^e + \boldsymbol{\varepsilon}^p \quad \text{with } \boldsymbol{\varepsilon} = \int_0^t \mathbf{d}dt; \quad \boldsymbol{\varepsilon}^e = \int_0^t \mathbf{d}^e dt; \quad \boldsymbol{\varepsilon}^p = \int_0^t \mathbf{d}^p dt. \tag{21}$$

The elastic strain $\boldsymbol{\varepsilon}^e$ is defined by Hooke law (the integral form of Eq. (13)):

$$\boldsymbol{\varepsilon}^e = \mathbb{S}^e \cdot \boldsymbol{\sigma}. \tag{22}$$

Within the deformation theory, the behavior is assumed to be elastoplastic throughout all loading and unloading stages. Consequently, the yield function $f(\boldsymbol{\sigma}, \sigma_Y) = \sigma_{\text{eq}} - \sigma_Y$ is always equal to 0. Furthermore, the plastic strain $\boldsymbol{\varepsilon}^p$ is given by the integral form of Eq. (15):

$$\boldsymbol{\varepsilon}^p = \varepsilon^p_{\text{eq}}\frac{\mathbb{I}_d \cdot \boldsymbol{\sigma}}{\sigma_{\text{eq}}}. \tag{23}$$

As Eq. (23) indicates, the normality law is violated when using the deformation theory. This aspect will be further illustrated and discussed in details in Sec. 3.1.3.

Through summation of Eqs. (22) and (23), we can establish the complete relationship between the stress and strain tensors. This relationship takes into consideration both elastic and plastic deformations:

$$\boldsymbol{\varepsilon} = \boldsymbol{\varepsilon}^e + \boldsymbol{\varepsilon}^p = \left[\mathbb{S}^e + \frac{\varepsilon^p_{\mathrm{eq}}}{\sigma_{\mathrm{eq}}}\mathbb{I}_d\right] \cdot \boldsymbol{\sigma}. \tag{24}$$

3.1.3. *Conceptual differences between the two constitutive frameworks*

Conceptually, the two constitutive frameworks differ in three key aspects:

(1) *Effect of deviation from proportional loading*: The deformation theory can be perceived as the integral form of the incremental flow theory, specifically under proportional loading conditions. As a result, for proportional loading scenarios, or when deviations from proportional loading are relatively slow and mild, both constitutive frameworks yield similar stress–strain responses. However, significant deviations from proportional loading histories, often arising due to pronounced non-linearities, such as substantial deformations, distortions, plastic behavior and contact phenomena, result in distinct predictions between the two frameworks. In situations characterized by severe deviations from proportional loading, the flow theory of plasticity may lead to rapid changes in plastic strain increments and consequently, distinct stress–strain responses compared to the deformation theory.

(2) *Difference in the loading stage*: Figure 1(a) provides a clear illustration of the stress–strain curves $\sigma_{\mathrm{eq}} - \varepsilon^p_{\mathrm{eq}}$, showcasing their identical nature for both models throughout the elastoplastic loading stage. Nonetheless, a substantial

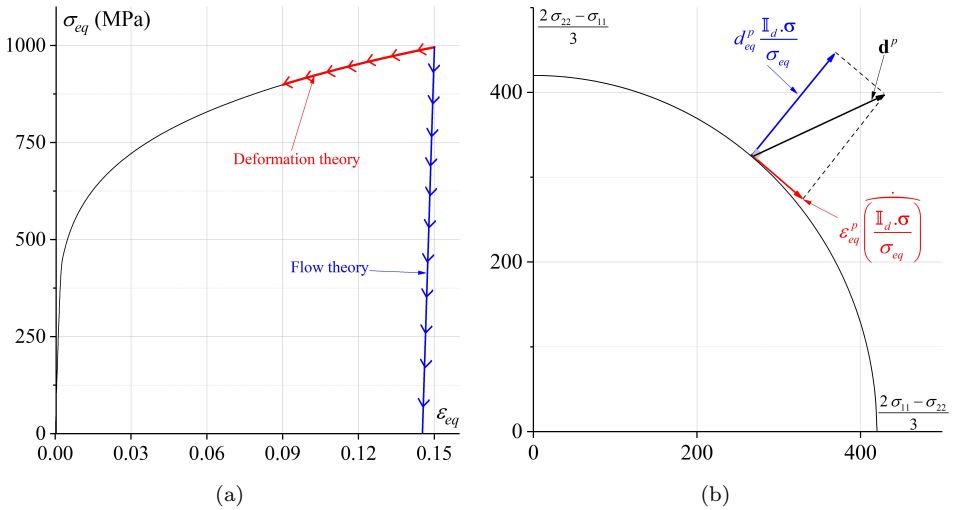

Fig. 1. Differences between the deformation theory and flow theory of plasticity: (a) Loading/Unloading history; (b) Plastic flow rule.

difference in their behavior becomes apparent under the unloading stage. During this subsequent stage, when the deformation theory is applied, the material consistently follows the same loading curve, indicating a sustained material response throughout the unloading process. In contrast, when employing the flow theory, the unloading process takes on an elastic nature, suggesting a different behavior altogether. This discrepancy in behavior during the unloading stage induces significant implications that will help understand the structural response and subsequent stability analysis of metal structures.

(3) *Violation of the normality law*: The normality law, which assumes that the plastic strain rate remains normal to the yield surface during plastic loading, holds true only for the flow theory of plasticity. However, for the deformation theory of plasticity, this normality law is not satisfied. Indeed, by taking the time derivative of Eq. (23), we obtain the following expression for $\mathbf{d}^p$:

$$\mathbf{d}^p = d^p_{\mathrm{eq}} \frac{\mathbb{I}_d \cdot \boldsymbol{\sigma}}{\sigma_{\mathrm{eq}}} + \varepsilon^p_{\mathrm{eq}} \left(\dot{\widehat{\frac{\mathbb{I}_d \cdot \boldsymbol{\sigma}}{\sigma_{\mathrm{eq}}}}} \right). \tag{25}$$

The first part of Eq. (25) (i.e., $(d^p_{\mathrm{eq}}/\sigma_{\mathrm{eq}})\mathbb{I}_d \cdot \boldsymbol{\sigma}$) is normal to the yield surface and is identical to the normality law given by Eq. (15). The second part (i.e., $\varepsilon^p_{\mathrm{eq}}(\dot{\widehat{\mathbb{I}_d \cdot \boldsymbol{\sigma}/\sigma_{\mathrm{eq}}}})$) leads to a deviation from the normality law, as schematically shown in Fig. 1(b). This deviation produces a destabilizing effect, which promotes the occurrence of elastoplastic buckling. The consequences of this deviation on the evolution of the components of the elastoplastic tangent modulus and on the onset of elastoplastic buckling will be highlighted in Secs. 3.2 and 4, respectively.

Historically, the deformation theory has been used in the context of plastic buckling problems due to the incapacity of the classical flow theory to predict critical buckling loads at realistic levels, as clearly shown in several scenarios. This observation, known as 'the plastic buckling paradox', has been confirmed in a number of well-established plastic buckling problems, such as the cruciform column problem examined in detail in Hutchinson and Budiansky [1976], and also referenced in Hutchinson [1970], Sewell [1973] and Sewell [1974]. Despite the conceptual drawbacks pointed out above, it has been demonstrated in several contributions that the deformation theory allows for the prediction of finite critical loads, which generally comply with experimental results.

3.2. *Numerical implementation*

Within the context of FEM, the constitutive equations detailed in Sec. 3.1 are incrementally integrated using implicit integration schemes to ensure numerical stability during the FE computations. The four-node quadrilateral shell element S4 of ABAQUS is used to discretize the various structures studied in this paper. Each node of this element has six degrees of freedom (three displacements and three rotations) enabling an accurate consideration of the membrane strain. Due to its

reliability and efficiency, this finite element has been widely used for the prediction of buckling of thin and thick structures [Shamass *et al.*, 2014; Nasikas *et al.*, 2022]. A plane-stress projected formulation is adopted in the following developments to easily manage the plane-stress constraint. This formulation, which is restricted to the plane-stress space, involves only the in-plane stresses and strains, as the out-of-plane strains may be computed *a posteriori* [Nguyen *et al.*, 2020]. Hence, during each time increment $I_\Delta = [t_n, t_{n+1}]$ and at every integration (Gauss) point of the finite element mesh, the increment of the total in-plane strain tensor $\Delta\boldsymbol{\varepsilon}$ (2D tensor) is assumed to be known and constant over that increment. The primary objective of the proposed integration schemes is to update the different variables at the end of I_Δ and to calculate the in-plane elastoplastic tangent modulus $\mathbb{C}^{\text{ep}}$ required for the finite element convergence and elastoplastic buckling analysis. To simplify the notation, subscript t_{n+1} will be omitted in the following developments, with the understanding that all variables are evaluated at time t_{n+1}, unless explicitly specified otherwise (e.g., $\bullet_n$ means variable at time t_n). This convention streamlines the mathematical expressions and allows for easier comprehension of the subsequent developments. For clarity, the integration schemes for both constitutive models; namely, the flow theory of plasticity and the total deformation theory, will be presented separately in the following sections.

3.2.1. *Flow theory of plasticity*

To integrate the constitutive equations corresponding to the flow theory of plasticity, the return-mapping algorithm is used. As initial step of this algorithm, the 2D trial elastic stress $\boldsymbol{\sigma}^{\text{Tr}}$ is computed using the following expression:

$$\boldsymbol{\sigma}^{\text{Tr}} = \boldsymbol{\sigma}_n + \mathbb{C}^e \cdot \Delta\boldsymbol{\varepsilon} \quad \text{with} \quad \mathbb{C}^e = (\mathbb{S}^e)^{-1} = \frac{E}{1-\nu^2}\begin{bmatrix} 1 & \nu & 0 \\ \nu & 1 & 0 \\ 0 & 0 & \dfrac{1-\nu}{2} \end{bmatrix}. \tag{26}$$

If the equivalent trial stress $\sigma_{\text{eq}}^{\text{Tr}} (= \sqrt{\boldsymbol{\sigma}^{\text{Tr}T} \cdot \mathbb{I}_d \cdot \boldsymbol{\sigma}^{\text{Tr}}})$ is smaller than the yield stress at the beginning of the time increment σ_{Yn} (i.e., $\sigma_{\text{eq}}^{\text{Tr}} < \sigma_{Yn}$), the behavior is fully elastic during the time increment I_Δ. Therefore, the material undergoes purely elastic deformation (this case is only encountered during elastic unloading), and no plastic strain accumulates during this time step:

$$\boldsymbol{\sigma} = \boldsymbol{\sigma}^{\text{Tr}}; \quad \varepsilon_{\text{eq}}^p = \varepsilon_{eqn}^p. \tag{27}$$

Otherwise, the material behavior becomes elastoplastic. In this case, the increment of the total strain $\Delta\boldsymbol{\varepsilon}$ should be split into its elastic and plastic components:

$$\Delta\boldsymbol{\varepsilon} = \Delta\boldsymbol{\varepsilon}^e + \Delta\boldsymbol{\varepsilon}^p. \tag{28}$$

The increment of the plastic strain $\Delta\boldsymbol{\varepsilon}^p$ is defined by the incremental form of Eq. (15):

$$\Delta\boldsymbol{\varepsilon}^p = \Delta\varepsilon^p_{\text{eq}} \frac{\mathbb{I}_d \cdot \boldsymbol{\sigma}}{\sigma_{\text{eq}}}. \tag{29}$$

Since the von Mises criterion is employed to model the yield surface, the following equality holds [Ben Bettaieb *et al.*, 2011]:

$$\frac{\boldsymbol{\sigma}}{\sigma_{\text{eq}}} = \frac{\boldsymbol{\sigma}^{\text{Tr}}}{\sigma^{\text{Tr}}_{\text{eq}}}. \tag{30}$$

Thus, the combination of Eqs. (29) and (30) results in

$$\Delta\boldsymbol{\varepsilon}^p = \Delta\varepsilon^p_{\text{eq}} \frac{\mathbb{I}_d \cdot \boldsymbol{\sigma}^{\text{Tr}}}{\sigma^{\text{Tr}}_{\text{eq}}}. \tag{31}$$

As $\boldsymbol{\sigma}^{\text{Tr}}$ and $\sigma^{\text{Tr}}_{\text{eq}}$ are known, tensor $\Delta\boldsymbol{\varepsilon}^p$ can be determined once $\Delta\varepsilon^p_{\text{eq}}$ is known.

On the other hand, the Cauchy stress tensor $\boldsymbol{\sigma}$ can be determined from the following incremental expression:

$$\boldsymbol{\sigma} = \boldsymbol{\sigma}_n + \mathbb{C}^e \cdot (\Delta\boldsymbol{\varepsilon} - \Delta\boldsymbol{\varepsilon}^p). \tag{32}$$

As tensor $\Delta\boldsymbol{\varepsilon}$ is known and $\Delta\boldsymbol{\varepsilon}^p$ depends only on the scalar unknown $\Delta\varepsilon^p_{\text{eq}}$, tensor $\boldsymbol{\sigma}$ (and subsequently its equivalent counterpart σ_{eq}) will be completely determined when $\Delta\varepsilon^p_{\text{eq}}$ is computed. Therefore, the updated Cauchy stress tensor is solely dependent on the scalar unknown $\Delta\varepsilon^p_{\text{eq}}$:

$$\boldsymbol{\sigma} \hat{=} \boldsymbol{\sigma}(\Delta\varepsilon^p_{\text{eq}}) \quad \text{and} \quad \sigma_{\text{eq}} \hat{=} \sigma_{\text{eq}}(\Delta\varepsilon^p_{\text{eq}}). \tag{33}$$

Furthermore, the yield stress σ_Y defined in Eq. (19) can be expressed as a function of $\Delta\varepsilon^p_{\text{eq}}$:

$$\sigma_Y = \sigma_0 \left[\frac{E\left(\varepsilon^p_{eqn} + \Delta\varepsilon^p_{\text{eq}}\right)}{K\sigma_0} \right]^{1/c}, \tag{34}$$

where $\varepsilon^p_{\text{eq}}$ and σ_Y are equal to 0 at the beginning of the loading.

As the behavior is elastoplastic from the beginning of the loading, the increment $\Delta\varepsilon^p_{\text{eq}}$ is strictly positive and the yield function f, introduced in Eq. (18), is necessarily equal to 0:

$$f\left(\boldsymbol{\sigma}, \sigma_Y\right) = \sigma_{\text{eq}} - \sigma_Y = 0, \tag{35}$$

By analyzing Eqs. (33) and (34), it comes obvious that the unique unknown variable on which σ_{eq} and σ_Y depend is $\Delta\varepsilon^p_{\text{eq}}$. This implies that σ_{eq} and σ_Y are no longer primary unknowns of the yield function f, but rather functions of $\Delta\varepsilon^p_{\text{eq}}$. Consequently, the yield function f can be completely expressed in terms of $\Delta\varepsilon^p_{\text{eq}}$:

$$f\left(\sigma, \sigma_Y\right) \hat{=} f\left(\Delta\varepsilon^p_{\text{eq}}\right) = 0. \tag{36}$$

Once $\Delta\varepsilon^p_{\text{eq}}$ is determined by solving the non-linear Eq. (36), $\Delta\boldsymbol{\varepsilon}^p$ and then $\boldsymbol{\sigma}$ can be easily computed from Eqs. (31) and (32), respectively. Consequently, solving

Eq. (36) enables a complete solution of the flow theory constitutive equations. Technical details about the solution of this equation by the Newton–Raphson iterative scheme are provided in Appendix A.

The elastoplastic tangent modulus $\mathbb{C}^{\text{ep}}$ should be evaluated after solving the above constitutive equations. To ensure the consistency between the finite element computations and the Hill loss of uniqueness criterion, the analytical tangent modulus should be implemented at the end of the UMAT instead of the (algorithmic) consistent one, usually used to ensure quadratic convergence [Zhu *et al.*, 2022]. Based on our earlier observations in Zhu *et al.* [2022], the use of the analytical tangent modulus does not compromise the effective and efficient finite element convergence. In fact, typically, only one iteration is required to achieve convergence at each time increment. The analytical tangent modulus $\mathbb{C}^{\text{ep}}$ allows the stress rate $\dot{\boldsymbol{\sigma}}$ to be related to the strain rate $\mathbf{d}$:

$$\dot{\boldsymbol{\sigma}} = \mathbb{C}^{\text{ep}} \cdot \mathbf{d}. \tag{37}$$

To determine this tangent modulus, Eq. (20) should be reformulated as follows:

$$\mathbf{d} = \mathbb{S}^e \cdot \dot{\boldsymbol{\sigma}} + d^p_{\text{eq}} \frac{\mathbb{I}_d \cdot \boldsymbol{\sigma}}{\sigma_{\text{eq}}} = \mathbb{S}^e \cdot \dot{\boldsymbol{\sigma}} + \frac{\dot{\sigma}_{\text{eq}}}{\sigma_{\text{eq}}} \frac{d^p_{\text{eq}}}{\dot{\sigma}_{\text{eq}}} \mathbb{I}_d \cdot \boldsymbol{\sigma} = \mathbb{S}^e \cdot \dot{\boldsymbol{\sigma}} + \frac{\dot{\sigma}_{\text{eq}}}{\sigma_{\text{eq}}} \frac{1}{h} \mathbb{I}_d \cdot \boldsymbol{\sigma} \tag{38}$$

with h the hardening slope equal to $d\sigma_{\text{eq}}/d^p_{\text{eq}}$. For the current hardening model, h is defined by the following expression:

$$h = \frac{\sigma_0 (E \varepsilon^p_{\text{eq}})^{\frac{1}{c}}}{c \varepsilon^p_{\text{eq}} (K \sigma_0)^{\frac{1}{c}}}. \tag{39}$$

The rate of the equivalent stress $\dot{\sigma}_{\text{eq}}$ can be determined as follows:

$$\dot{\sigma}_{\text{eq}} = \left[\frac{\partial \sigma_{\text{eq}}}{\partial \boldsymbol{\sigma}} \right] \cdot \dot{\boldsymbol{\sigma}} = \frac{[\mathbb{I}_d \cdot \boldsymbol{\sigma}] \cdot \dot{\boldsymbol{\sigma}}}{\sigma_{\text{eq}}}. \tag{40}$$

Inserting Eq. (40) into Eq. (38) leads to the following expression:

$$\mathbf{d} = \mathbb{S}^e \cdot \dot{\boldsymbol{\sigma}} + \frac{(\mathbb{I}_d \cdot \boldsymbol{\sigma}) \otimes (\mathbb{I}_d \cdot \boldsymbol{\sigma})}{h \sigma^2_{\text{eq}}} \cdot \dot{\boldsymbol{\sigma}} = \left[\mathbb{S}^e + \frac{(\mathbb{I}_d \cdot \boldsymbol{\sigma}) \otimes (\mathbb{I}_d \cdot \boldsymbol{\sigma})}{h \sigma^2_{\text{eq}}} \right] \cdot \dot{\boldsymbol{\sigma}}. \tag{41}$$

The tangent modulus $\mathbb{C}^{\text{ep}}$ can be obtained by inverting Eq. (41):

$$\mathbb{C}^{\text{ep}} = \left[\mathbb{S}^e + \frac{(\mathbb{I}_d \cdot \boldsymbol{\sigma}) \otimes (\mathbb{I}_d \cdot \boldsymbol{\sigma})}{h \left(\sigma_{\text{eq}}\right)^2} \right]^{-1}. \tag{42}$$

3.2.2. *Deformation theory of plasticity*

Equation (30) remains valid for the deformation theory of plasticity. Hence, the plastic strain $\boldsymbol{\varepsilon}^p$, given by Eq. (23), can be defined as a function of the known

vector $\boldsymbol{\sigma}^{\mathrm{Tr}}/\sigma_{\mathrm{eq}}^{\mathrm{Tr}}$ as follows:

$$\boldsymbol{\varepsilon}^p = \varepsilon_{\mathrm{eq}}^p \frac{\mathbb{I}_d \cdot \boldsymbol{\sigma}^{\mathrm{Tr}}}{\sigma_{\mathrm{eq}}^{\mathrm{Tr}}}. \tag{43}$$

Then, the stress tensor $\boldsymbol{\sigma} = \mathbb{C}^e \cdot (\boldsymbol{\varepsilon} - \boldsymbol{\varepsilon}^p)$ and hence its equivalent value σ_{eq} can be determined if $\varepsilon_{\mathrm{eq}}^p$ is known. Also, the yield stress σ_Y depends on the unique unknown $\varepsilon_{\mathrm{eq}}^p$. Therefore, to solve the deformation theory constitutive equations, it is sufficient to determine $\varepsilon_{\mathrm{eq}}^p$ by solving the following scalar equation:

$$f\left(\boldsymbol{\sigma}, \sigma_Y\right) = \sigma_{\mathrm{eq}} - \sigma_Y \mathrel{\hat{=}} f\left(\varepsilon_{\mathrm{eq}}^p\right) = 0. \tag{44}$$

As for Eq. (36), the non-linear Eq. (44) is solved by the Newton–Raphson method for the unknown $\varepsilon_{\mathrm{eq}}^p$. An algorithm very similar to the one presented in Appendix A is followed to solve Eq. (44).

Similar to the flow theory, the analytical expression of the elastoplastic tangent modulus $\mathbb{C}^{\mathrm{ep}}$ should be determined for the deformation theory. As a departure point to determine this modulus, Eq. (24) should be expressed in its rate form

$$\begin{aligned}
\mathbf{d} = \mathbf{d}^e + \mathbf{d}^p &= \mathbb{S}^e \cdot \dot{\boldsymbol{\sigma}} + \frac{d_{\mathrm{eq}}^p}{\sigma_{\mathrm{eq}}}(\mathbb{I}_d \cdot \boldsymbol{\sigma}) - \frac{\varepsilon_{\mathrm{eq}}^p \dot{\sigma}_{\mathrm{eq}}}{(\sigma_{\mathrm{eq}})^2}(\mathbb{I}_d \cdot \boldsymbol{\sigma}) + \frac{\varepsilon_{\mathrm{eq}}^p}{\sigma_{\mathrm{eq}}}(\mathbb{I}_d \cdot \dot{\boldsymbol{\sigma}}), \\
&= \mathbb{S}^e \cdot \dot{\boldsymbol{\sigma}} + \frac{\dot{\sigma}_{\mathrm{eq}}}{\sigma_{\mathrm{eq}}}\left(\frac{d_{\mathrm{eq}}^p}{\dot{\sigma}_{\mathrm{eq}}} - \frac{\varepsilon_{\mathrm{eq}}^p}{\sigma_{\mathrm{eq}}}\right)(\mathbb{I}_d \cdot \boldsymbol{\sigma}) + \frac{\varepsilon_{\mathrm{eq}}^p}{\sigma_{\mathrm{eq}}}(\mathbb{I}_d \cdot \dot{\boldsymbol{\sigma}}), \\
&= \mathbb{S}^e \cdot \dot{\boldsymbol{\sigma}} + \frac{\dot{\sigma}_{\mathrm{eq}}}{\sigma_{\mathrm{eq}}}\left(\frac{1}{h} - \frac{1}{E_s}\right)(\mathbb{I}_d \cdot \boldsymbol{\sigma}) + \frac{\varepsilon_{\mathrm{eq}}^p}{\sigma_{\mathrm{eq}}}(\mathbb{I}_d \cdot \dot{\boldsymbol{\sigma}}).
\end{aligned} \tag{45}$$

For the Ramberg–Osgood hardening model used in this work, the hardening slope $h = \dot{\sigma}_{\mathrm{eq}}/d_{\mathrm{eq}}^p$ is defined by Eq. (39), while the secant modulus $E_s = \sigma_{\mathrm{eq}}/\varepsilon_{\mathrm{eq}}^p$ is equal to ch. By introducing the expression of $\dot{\sigma}_{\mathrm{eq}}$ given by Eq. (40) into Eq. (45), the tangent modulus $\mathbb{C}^{\mathrm{ep}}$ can be determined as follows:

$$\begin{aligned}
\mathbf{d} &= \left[\mathbb{S}^e + \frac{\mathbb{I}_d}{E_s} + \left(\frac{1}{h} - \frac{1}{E_s}\right)\frac{(\mathbb{I}_d \cdot \boldsymbol{\sigma}) \otimes (\mathbb{I}_d \cdot \boldsymbol{\sigma})}{(\sigma_{\mathrm{eq}})^2}\right] \cdot \dot{\boldsymbol{\sigma}} \\
\Leftrightarrow \mathbb{C}^{\mathrm{ep}} &= \left[\mathbb{S}^e + \frac{\mathbb{I}_d}{ch} + \left(\frac{1}{h} - \frac{1}{ch}\right)\frac{(\mathbb{I}_d \cdot \boldsymbol{\sigma}) \otimes (\mathbb{I}_d \cdot \boldsymbol{\sigma})}{(\sigma_{\mathrm{eq}})^2}\right]^{-1}.
\end{aligned} \tag{46}$$

It is worth noting that the two tangent moduli corresponding to the two constitutive frameworks (Eqs. (42) and (46)) have some differences in their mathematical structures (despite the similarities observed in the stress–strain curves presented in Fig. 1(a)). This distinction arises from the conceptual differences discussed in Sec. 3.1.3. To highlight these differences, we have simulated an equibiaxial in-plane compression test applied on a material point and defined by the

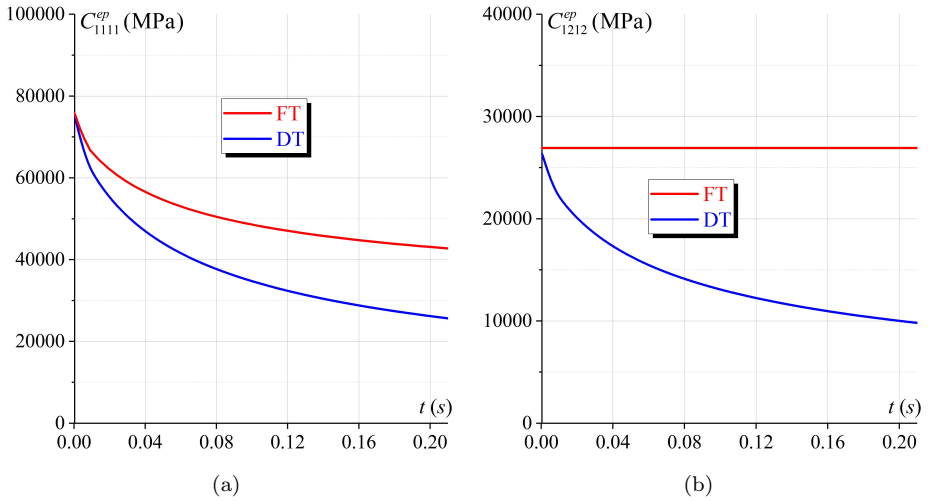

Fig. 2. Evolution of the most relevant components of the elastoplastic tangent moduli $\mathbb{C}^{\text{ep}}$ versus t: (a) C^{ep}_{1111}; (b) C^{ep}_{1212}.

following strain state:

$$\boldsymbol{\varepsilon} = \begin{bmatrix} -d_{11}t & 0 \\ 0 & -d_{11}t \end{bmatrix} \quad \text{with } d_{11} = 1s^{-1}. \tag{47}$$

The loading is applied until time $t = 0.2\,s$. As depicted in Fig. 2(a), the two frameworks yield the same value for the component C^{ep}_{1111} at the beginning of the loading. However, the value of this component decreases for both frameworks during plastic deformation, with different decrease rates. Conversely, the shearing component C^{ep}_{1212} remains constant and keeps its elastic value for the flow theory, as demonstrated in Fig. 2(b). A notably different trend is observed when the deformation theory is used. In this latter case, the shearing component C^{ep}_{1212} is substantially reduced during the deformation process. This variance in terms of behavior naturally arises due to the violation of the normality law, as highlighted in Fig. 1(b). The main destabilizing factor that triggers bifurcation [Ben Bettaieb and Abed-Meraim, 2015] and promotes early elastoplastic buckling is the reduction of this shearing component, as demonstrated in further details in Sec. 4.2.

4. Numerical Predictions

4.1. *Square plates*

4.1.1. *Finite element model*

In the simulations presented in this section, attention is focused on square plates, as illustrated in Fig. 3. The length a of each plate is set to $200\,mm$ and its thickness

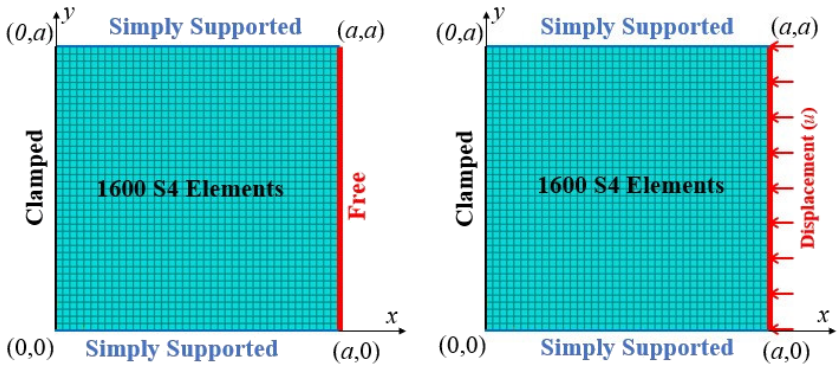

Fig. 3. Description of the FE model: (a) Initial boundary conditions; (b) Applied compression loading.

is denoted as t. To explore the influence of the slenderness ratio on the critical buckling stress magnitude, three values of t/a (the inverse of the slenderness ratio, which is commonly used as a characteristic geometric parameter) are employed to obtain the subsequent results: 0.025; 0.05; and 0.075. As shown in Fig. 3(a), the plate is initially subjected to the following boundary conditions: simply supported (S) along the edges $y = 0$ and $y = a$, clamped (C) along the edge $x = 0$ and Free (F) along the edge $x = a$. These boundary conditions, denoted as CSFS, are chosen to enable comparisons with the findings published in Wang *et al.* [2001]. The plate is subjected to a uniaxial compression test in the x-direction by imposing a uniform displacement u, as depicted in Fig. 3(b). To establish an appropriate mesh discretization of the plate, we have performed a mesh sensitivity study. From the results of this analysis, we have concluded that a structured mesh consisting of 1600 elements (comprising 1681 nodes) represents a reasonable compromise between simulation accuracy and computational efficiency. Consequently, we have adopted this mesh configuration for all the simulations conducted in this section.

To ensure an accurate estimation of the critical buckling loads, the '*nlgeom*' option should be activated in the '*Step*' section of the input file, as explained in Box 1. Furthermore, it is essential to account for the transverse shear effect, as neglecting this aspect leads to an overestimation of the buckling loads [Wang, 1995]. Throughout all simulations presented in Sec. 4.1, a shear correction factor $k_c = \sqrt{5/6}$ is used to preserve consistency with the Mindlin–Reissner plate theory. This choice aligns with the recommendations provided in references [Wang *et al.*, 2001; Reinssner, 1945].

To assess the reliability and precision of the proposed computational strategy, our predictions are compared to those published by Wang *et al.* [2001], based on an analytical methodology. To facilitate this comparative analysis, the incremental stress factor Φ is assessed at the end of each finite element increment. This factor

is defined by the following formula:

$$\Phi = \frac{12a^2(1-\nu^2)\sigma}{E\pi^2 t^2}, \tag{48}$$

where σ is the compressive stress applied along the edge $x = a$, while E and ν are the elasticity parameters.

4.1.2. *Elastic predictions*

The developed numerical strategy is firstly applied to assess the influence of the ratio t/a on the elastic buckling of square plates. For this purpose, the DT framework is used with a nominal yield strength σ_0 is set to 1 GPa. This high value is chosen to ensure that the buckling load falls dominantly within the elastic range (i.e., plastic deformation remains very small compared to the elastic one). It is worth noting that, in this context, both the FT and DT frameworks yield identical results. The Young modulus E and Poisson ratio ν are set to 70 GPa and 0.3, respectively. To conduct a comprehensive analysis of the impact of the ratio t/a, Fig. 4 depicts the evolution of the smallest eigenvalue $\lambda_{\min}$ of the reduced stiffness matrix $\tilde{\mathbf{K}}$ normalized by its initial value λ_0 (evaluated at the first finite element increment), against the stress factor Φ^{FE} determined by our strategy spanning a loading interval around the buckling point. As shown in Fig. 4, the evolution of the ratio $\lambda_{\min}/\lambda_0$ exhibits a slight decrease prior to the occurrence of elastic buckling, while keeping a positive value. Then, this ratio plunges to negative values passing through the bifurcation point, which corresponds to a zero eigenvalue. The buckling stress factor at this point $\Phi_{\mathrm{cr}}^{\mathrm{FE}}$ is computed via linear interpolation between the last positive and first negative eigenvalues. As clearly shown in this figure, the increase of the plate

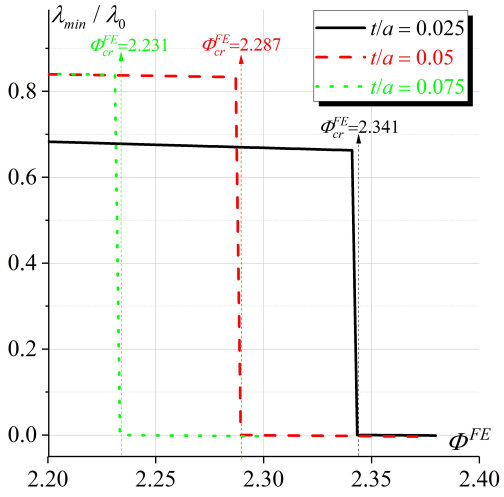

Fig. 4. Evolution of the smallest eigenvalue $\lambda_{\min}$ normalized by its initial value λ_0 versus the stress factor Φ^{FE}.

thickness leads to a decrease of the buckling stress factor Φ_{cr}^{FE}, which confirms the trends reported in Wang *et al.* [2001], Zhang and Wang [2011] and Ruocco [2015].

The comparisons between the critical stress factors $\Phi_{cr^{Analy}}$ predicted by the analytical methodology provided in Wang *et al.* [2001], Φ_{cr}^{Buckle} predicted by the '*Buckle*' module of ABAQUS, and their counterparts Φ_{cr}^{FE} determined by our numerical strategy are presented in Table 1. These comparisons reveal good agreement between these various computational approaches. In fact, the most significant relative deviation between these approaches remains below 2%. Notably, the discrepancy between the results from the analytical approach and our numerical strategy expands as the plate thickness t increases. This observation is likely to be attributable to the important influence of transverse shear deformations, an effect that is particularly pronounced for thicker plates. Moreover, beyond the determination of the critical buckling stress, the developed computational strategy offers the possibility to provide the buckling mode shapes by computing the eigenvectors of the reduced stiffness matrix $\tilde{\mathbf{K}}$. Such buckling mode plots allow a deeper understanding of the underlying buckling mechanisms. The first buckling mode shapes, obtained from our numerical strategy, are illustrated in Table 1. To ensure consistent comparisons between the different approaches, the mode shapes determined by our new computational strategy are plotted with amplification in out-of-plane deflection, using the same amplification factor that is automatically applied to the outcomes from the '*Buckle*' module. It is of significance to emphasize that, regardless of the thickness-to-width ratio, plate buckling follows a consistent single half-wave pattern. This observation is in accordance with well-known literature, establishing that for square plates, the fundamental buckling mode presents as a single half-wave pattern [Timoshenko and Gere, 1961].

4.1.3. *Elastoplastic predictions*

In this section, the proposed strategy is applied to analyze the buckling behavior of elastoplastic plates. The elasticity parameters, boundary conditions and geometric dimensions used in Sec. 4.1.2 are again adopted in the present elastoplastic analysis. The hardening parameters K and σ_0 are set to 0.25 and 350 MPa, respectively. To highlight the influence of strain hardening on the onset of elastoplastic buckling, two extreme values of the hardening exponent are considered in the following simulations: 2 and 20. The critical stress factors Φ_{cr}^{FE} are predicted using the Flow Theory (FT) as well as the Deformation Theory (DT) presented in Secs. 3.2.1 and 3.2.2, respectively. Table 2 provides a comparative presentation of our evaluations alongside the analytical results presented in Wang *et al.* [2001], illustrating the critical stress factors for all the cases under examination. The analytical critical stress factors Φ_{cr}^{Analy} are computed based on Mindlin plate theory, using both the flow and deformation theories [Wang *et al.*, 2001]. In the latter theory of plasticity, the secant modulus S is introduced into the elastoplastic buckling governing equations. By taking this modulus to be equal to the elastic modulus E, the equations

Table 1. Effect of the thickness ratio t/a on the buckling stress factor and the corresponding mode shape for elastic square plates.

		Present work					
		'Buckle' module			New strategy		
t/a	$\Phi_{\rm cr}^{\rm Analy}$ [Wang *et al.*, 2001]	Mode shape	$\Phi_{\rm cr}^{\rm Buckle}$	$D_{\rm Analy}^{\rm Buckle}(\%)^{\rm a}$	Mode shape	$\Phi_{\rm cr}^{\rm FE}$	$D_{\rm Analy}^{\rm FE}(\%)$
0.025	2.336	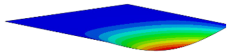	2.352	0.68	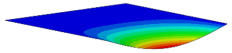	2.341	0.21
0.05	2.268	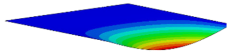	2.281	0.57	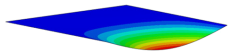	2.287	0.83
0.075	2.189	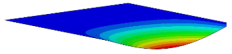	2.201	0.54	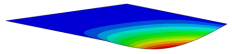	2.231	1.90

Note: [a]The relative deviation D_{M1}^{M2} is equal to the ratio $200(\Phi_{\rm cr}^{M2} - \Phi_{\rm cr}^{M1})/\Phi_{\rm cr}^{M2} + \Phi_{\rm cr}^{M1})$.

Table 2. Combined effect of the ratio t/a and the hardening exponent c on the buckling stress factor (with $E/\sigma_0 = 200$).

t/a	c	Const. model	$\Phi_{\rm cr}^{\rm Analy}$ [Wang *et al.*, 2001]	New strategy $\Phi_{\rm cr}^{\rm FE}$	$\Phi_{\rm Analy}^{\rm FE}(\%)$
0.025	2	FT	2.251	2.254	0.13
		DT	2.15	2.155	0.23
	20	FT	2.336	2.341	0.21
		DT	2.336	2.341	0.21
0.05	2	FT	2.022	2.025	0.14
		DT	1.767	1.781	0.78
	20	FT	1.976	1.968	−0.40
		DT	1.962	1.95	−0.61
0.075	2	FT	1.801	1.833	1.76
		DT	1.441	1.482	2.80
	20	FT	1.151	1.144	−0.61
		DT	1.002	1.007	0.49

derived from the deformation theory simplify to those obtained using the flow theory with Prandtl–Reuss equations. Regardless of the used theory, good agreement is shown for all the considered cases, which confirms the reliability of our strategy in the prediction of elastoplastic buckling behavior. The relative deviation between the analytical and numerical results increases with the thickness ratio, as already observed for elastic plates. The maximum discrepancy reaches approximately 2.8% for the thickest plate ($t/a = 0.075$).

For a more comprehensive evaluation of the reliability of our approach, the relationships between the buckling stress factor $\Phi_{\rm cr}$ and the ratio t/a are illustrated in Fig. 5. This graphical presentation effectively captures the trends obtained by our numerical predictions (represented by symbols ■), as compared to the analytical findings (depicted by lines). In particular, the numerical results closely reproduce the analytical trends. Therefore, it can be concluded that the slight differences between numerical and analytical results do not alter the reported conclusions on the effects of thickness and material parameters. For instance, the buckling stress factor decreases with the increase in the thickness ratio t/a. This decline is particularly pronounced with $c = 20$ for both plasticity theories. This result can be attributed to the effect of the hardening exponent c on the stress–strain relationship, as clearly shown in Eq. (19). Moreover, with the increase in the ratio t/a, the buckling stress factors obtained by both constitutive frameworks deviate more and more from their elastic counterparts. This observation can be explained by the fact that as the thickness increases, the plates undergo larger plastic strains prior to buckling, which in turn increases the gap between the predicted elastoplastic buckling loads and their elastic counterparts [Wang *et al.*, 2001; Zhang and Wang, 2011]. Turning to the effect of the constitutive framework, it can be clearly observed that the flow theory produces higher buckling stress factors, as compared to the deformation theory. This variance can be explained by the difference in the expressions of the tangent moduli corresponding to the flow theory (Eq. (42)) and deformation theory (Eq. (46)).

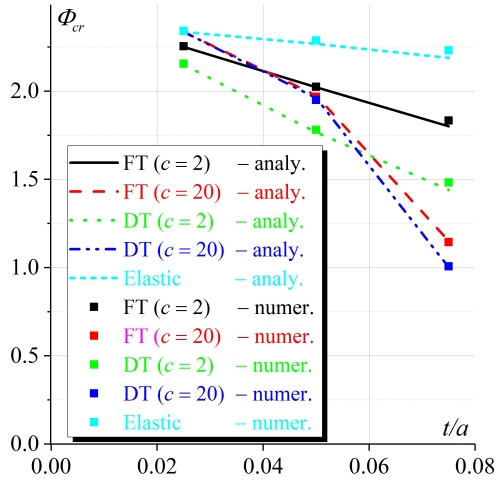

Fig. 5. Effect of the ratio t/a and the hardening exponent c on the buckling stress factor Φ_{cr}.

Particularly, the shearing component of the tangent modulus C^{ep}_{1212} decreases with the plastic deformation for the deformation theory, while it remains constant and equal to its elastic value for the flow theory, as shown in Fig. 2(b). This difference in the evolution of components of the elastoplastic tangent moduli leads to a difference in the magnitude of the buckling load.

Furthermore, as clearly shown in Fig. 5, the difference in the predictions yielded by the two constitutive frameworks amplifies with the increase in the plate thickness. This trend can also be related to the influence of the plate thickness on plastic yielding. As previously discussed in Sec. 3, higher plastic deformation increases the second component in the second part of Eq. (25), which in turn promotes deviation from the normality law. This deviation gives rise to a noticeable distinction between the two constitutive frameworks.

To better explore the effect of material parameters on the buckling behavior of thin plates ($t/a = 0.025$), additional simulations are conducted by employing different values of parameters c and E/σ_0. The obtained predictions are compared in Table 3 to the analytical results reported in Wang *et al.* [2001]. The relative deviation $D^{\mathrm{FE}}_{\mathrm{Analy}}$ spans between 0.05% and 0.82%, thereby confirming the accuracy of the developed computational strategy. Moreover, when $c = 20$ and $E/\sigma_0 = 200$, the buckling stress factors predicted by the two plasticity constitutive frameworks become equal, and coincide with the elastic buckling stress factor. This can be explained by the fact that, with such a high hardening exponent, the stress–strain behavior closely follows the elastic response, leading to buckling dominantly occurring within the elastic range. When c decreases or the ratio E/σ_0 increases, buckling occurs in the plastic range, with predicted buckling stresses falling below their elastic counterpart and exhibiting higher dependency on the plasticity constitutive framework. These trends are consistent with those reported by Wang [2004].

Table 3. Combined effect of material parameters E/σ_0 and c on the buckling stress factor ($t/a = 0.025$).

E/σ_0	c	Const. model	Φ_{cr}^{Analy} [Wang *et al.*, 2001]	New strategy Φ_{cr}^{FE}	$D_{Analy}^{FE}(\%)$
200	2	FT	2.251	2.254	0.13
		DT	2.15	2.155	0.23
	5	FT	2.332	2.341	0.38
		DT	2.329	2.31	−0.82
	20	FT	2.336	2.341	0.21
		DT	2.336	2.341	0.21
750	2	FT	2.097	2.086	−0.52
		DT	1.835	1.839	0.21
	5	FT	2.019	2.023	0.19
		DT	1.901	1.902	0.05
	20	FT	2.085	2.072	−0.62
		DT	2.071	2.066	−0.24

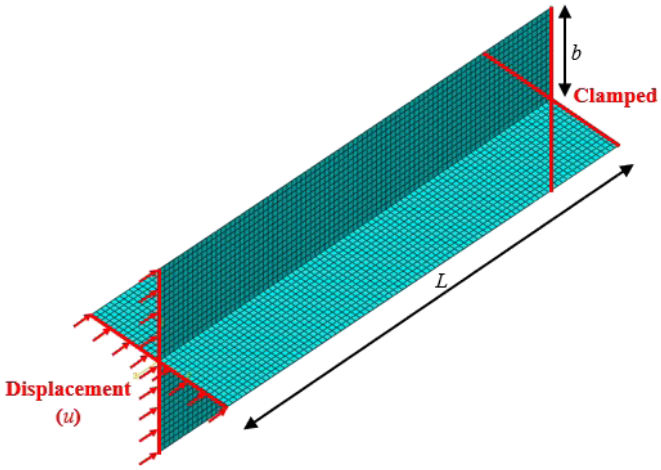

Fig. 6. Cruciform column: Geometry, boundary conditions and mesh discretization.

4.2. *Cruciform columns*

4.2.1. *Finite element model*

To further validate the proposed computational strategy, the buckling responses of cruciform columns are investigated. The geometry of the studied columns, the applied boundary conditions, and the mesh discretization are presented in Fig. 6. The column geometry is characterized by a length L, a cross-section dimension b, and a thickness t. For comparison purposes, the three specimens S1, S2 and S3 studied in Hopperstad *et al.* [1999] are considered in this section. The geometric parameters of these specimens, their mesh characteristics, and their material parameters are comprehensively detailed in Table 4.

Table 4. Geometric and material properties of the simulated columns [Guarracino and Simonelli, 2017] and mesh characteristics.

Spec.	b (mm)	L (mm)	t (mm)	E (GPa)	ν	σ_0 (MPa)	K	c	Elem. Nb.	Node. Nb.
S1	262.5	1500	25	69.7	0.3	131	1.064	23	4980	5124
S2	262.5	1500	25	67.9	0.3	267	0.509	45	4980	5124
S3	200	1500	24	65.13	0.3	178	0.733	16	4794	4940

To perform the elastoplastic buckling analyses, an axial compression loading is applied by imposing a displacement u on the column cross section, as depicted in Fig. 6. To assess the reliability of the proposed method in tracking the elastoplastic buckling, the two implemented constitutive frameworks are used in the different simulations (namely, the flow and deformation theories of plasticity). As for the simulations of Sec. 4.1, the shear correction factor k_c is set to $\sqrt{5/6}$ to ensure the consistency of our FE modeling with the Mindlin–Reissner plate theory.

4.2.2. *Numerical predictions*

To demonstrate the capabilities of our computational strategy, the predictions obtained from this strategy are compared in Table 5 to those published in Hopperstad *et al.* [1999], Guarracino and Simonelli [2017] and Lubliner [2008]. On the basis of these comparisons, the main following conclusions can be drawn:

- The torsional buckling of specimens S1, S2 and S3 is investigated on the basis of the classical analytical formulation of Lubliner [2008]. These specimens are assumed to be short columns with thin plate sections, which tend to buckle in the torsion mode under axial compression. In this case, the critical buckling stress is given by the following formula used in Lubliner [2008]:

$$\sigma_{\mathrm{cr}} = \bar{G}\left(\frac{t^2}{b^2}\right)^2, \tag{49}$$

  where the expression for modulus $\bar{G}$ depends on the used constitutive framework. It is equal to the elastic shear modulus $G = E/2(1+\nu)$ when the column is supposed to be purely elastic or when its elastoplastic behavior follows the flow theory. When the deformation theory of plasticity is used to model the column behavior, modulus $\bar{G}$ is equal to the secant shear modulus $G_s = E_s/(3 + (1 - 2\nu)E_s/E)$ (where E_s is the uniaxial secant modulus given by $\sigma_{\mathrm{eq}}/\varepsilon^p_{\mathrm{eq}}$). As shown in Lubliner [2008], the deformation theory exhibits good agreement with the experimental results, whereas the flow theory overestimates the buckling stress. This observation has led to the well-known elastoplastic buckling paradox. For columns S1 and S3, buckling occurs in the elastoplastic range. In such cases, the critical buckling loads predicted by our computational strategy $\sigma_{\mathrm{cr}}^{\mathrm{FE}}$ are consistent with those obtained by the analytical formulation $\sigma_{\mathrm{cr}}^{\mathrm{Analy1}}$ determined by Eq. (49)

Table 5. Buckling stress factors for cruciform columns.

Spec.	Const. model	New strategy σ_{cr}^{FE}(MPa)	σ_{cr}^{Analy1} (MPa) [Lubliner, 2008]	D_{Analy1}^{FE}(%)	σ_{cr}^{Analy2} (MPa) [Guarracino and Simonelli, 2017]	D_{Analy2}^{FE}(%)
S1	Elastic	237.28	243.15	2.44	***	***
	FT	126.98	243.15	62.77	128.73	1.37
	DT	126.57	129.06	1.95	128.47	1.49
S2	Elastic	231.15	236.87	2.44	***	***
	FT	231.18	236.84	2.43	232.02	0.36
	DT	230.95	236.24	2.27	232.78	0.79
	Elastic	350.79	360.72	2.79	***	***
S3	FT	164.14	360.72	74.91	177.75	7.97
	DT	163.81	179.82	9.32	177.75	8.16

Spec.	Const. model	New strategy σ_{cr}^{FE}(MPa)	σ_{cr}^{Num} (MPa) [Guarracino and Simonelli, 2017]	D_{Num}^{FE}(%)	σ_{cr}^{Exp} (MPa) [Hopperstad *et al.*, 1999]	D_{Exp}^{FE}(%)
S1	Elastic	237.28	***	***	124	62.71
	FT	126.98	134.04	5.41		2.38
	DT	126.57	128.67	1.65		2.05
S2	Elastic	231.15	***	***	218	5.85
	FT	231.18	240.18	3.82		5.87
	DT	230.95	239.62	3.69		5.77
S3	Elastic	350.79	***	***	***	***
	FT	164.14	191.55	15.42		***
	DT	163.81	179.38	9.07		***

when the mechanical behavior is modeled either by a purely elastic model or by the deformation theory of plasticity. On the contrary, our numerical predictions based on the flow theory of plasticity are about $1:2$ of the analytical ones given by Eq. (49) for columns S1 and S3. These results highlight the inadequacy of the analytical model Eq. (49) to predict the elastoplastic buckling through the flow theory. As to column S2, buckling is reached in the elastic range. Consequently, the various constitutive frameworks lead to nearly identical critical buckling loads.

- Guarracino and Simonelli [2017] have addressed the elastoplastic buckling paradox by introducing an initial imperfection within the columns and by postulating that, for the flow theory, the modulus $\bar{G}$ in Eq. (49) is equal to the tangent shear modulus $G_t = E_t/(3 + (1 - 2\nu)E_t/E)$ (where E_t is the uniaxial tangent modulus given by $d\sigma_{\mathrm{eq}}/d\varepsilon^p_{\mathrm{eq}}$). For the deformation theory, the expression of $\bar{G} = G_s$ holds the same. The analytical results $\sigma_{\mathrm{cr}}^{\mathrm{Analy2}}$ displayed in Table 5 are obtained by the analytical approach presented in Guarracino and Simonelli [2017], with an initial imperfection size of $1/100$ of the flange thickness. It can be seen that our findings align more closely with these results, as the maximum error is about 8%. This maximum error, which is displayed for column S3 with the thicker plate section ($t/b = 0.12$), can be attributed to the fact that the analytical model is based on thin plate theory. When modeling thick plates, neglecting transverse shear deformation will give rise to overestimation of the buckling load [Wang, 1995]. Hence, our FE model that applies the Mindlin–Reissner plate theory predicts lower stress values than those of the analytical formulation.
- Guarracino and Simonelli [2017] have also developed a non-linear FE model strategy based on the Riks method to predict the critical buckling stress of cruciform columns (denoted as $\sigma_{\mathrm{cr}}^{\mathrm{Num}}$ in Table 5), by assuming the pre-existence of an initial imperfection. Our numerical results, obtained by the Newton–Raphson method, for perfect columns (i.e., with no imperfection), and accounting for the transverse shear effect, display reasonable agreement with the numerical findings of Guarracino and Simonelli [2017]. Once again, the maximum discrepancy is observed for column S3 with the thicker plate section. This proves the importance of considering the transverse shear effect.
- Experimental measurements of buckling stresses have been recorded for columns S1 and S2 by Hopperstad *et al.* [1999], using a universal testing machine under quasi-static loading conditions. The results of this experimental investigation (designated as $\sigma_{\mathrm{cr}}^{\mathrm{Exp}}$ in Table 5) are compared to our numerical predictions. It is noteworthy that our results are fully consistent with the experimental ones. As the buckling of column S1 occurs in the elastoplastic range, both theories of plasticity give critical buckling loads in good agreement with experimental results, with a maximum difference of about 2.5%. On the other hand, the elastic framework in this case overestimates the critical buckling load. For column S2 that buckles prior to plastic deformation, the maximum difference between numerical and experimental results is about 6%. It should be noted that the experimental

values of the critical buckling loads are lower than the numerical ones, due to the unavoidable imperfections in actual specimens.

All of these comparisons definitely confirm the reliability of the proposed approach and the accuracy of the algorithmic developments and associated numerical tools in predicting the elastoplastic buckling of shell structures.

5. Summary and Conclusions

In this study, a novel computational strategy has been introduced within the framework of ABAQUS/Standard FE code to predict the occurrence of elastoplastic buckling in shell structures. The development of this strategy has involved the implementation of two distinct constitutive frameworks as User MATerial subroutines within the ABAQUS environment: the incremental flow theory and the total deformation theory of plasticity. To predict the critical buckling loads and the associated buckling modes, a Python script has been specifically designed to exploit the outcomes derived from finite element simulations. Particular attention has been paid to both the effectiveness and reliability of each constituent element within this computational strategy, in particular the User MATerial subroutines (UMATs) and the Python script.

The accuracy and robustness of the proposed strategy have been exhaustively assessed through extensive comparisons with a set of various and representative benchmark problems previously documented in the literature. As an outcome, this contribution offers useful reference guidelines to ABAQUS/Standard users, providing them with valuable insights into the prediction of elastoplastic buckling phenomena. It is worth noting that, with some suitable adaptations, the computational strategy presented here could also be applied in combination with other commercial finite element software packages. Moving forward, the proposed approach is intended to be extended to investigate more elaborate structures (with complex geometries and boundary conditions) and to analyze the influence of more advanced constitutive models [Zhu *et al.*, 2023; Ben Bettaieb and Abed-Meraim, 2021; Paux *et al.*, 2020; Jedidi *et al.*, 2020; Ben Bettaieb and Abed-Meraim, 2017a,b] on elastoplastic buckling initiation.

Appendinx A. Iterative Solution of Eq. (36)

To solve the flow theory constitutive equations, the non-linear Eq. (36) should be solved by the Newton–Raphson iterative scheme, where the unique scalar unknown reduces to the increment of the equivalent plastic strain $\Delta\varepsilon^{p}_{\mathrm{eq}}$. The application of the Newton–Raphson approach to Eq. (36) results in the following iterative formulation:

$$\Delta\varepsilon^{p(i+1)}_{\mathrm{eq}} = \Delta\varepsilon^{p(i)}_{\mathrm{eq}} - \frac{f\left(\Delta\varepsilon^{p(i)}_{\mathrm{eq}}\right)}{\mathcal{J}\left(\Delta\varepsilon^{p(i)}_{\mathrm{eq}}\right)}, \tag{A.1}$$

where $\mathcal{J}$ is equal to $\partial f/\partial \Delta\varepsilon^p_{\rm eq}$. Its analytical expression is determined by the following developments:

$$\mathcal{J}\left(\Delta\varepsilon^p_{\rm eq}\right) = \frac{\partial\sigma_{\rm eq}}{\partial\Delta\varepsilon^p_{\rm eq}} - \frac{\partial\sigma_Y}{\partial\Delta\varepsilon^p_{\rm eq}}; \quad \frac{\partial\sigma_Y}{\partial\Delta\varepsilon^p_{\rm eq}} = \frac{\sigma_Y}{c\left(\varepsilon^p_{eqn} + \Delta\varepsilon^p_{\rm eq}\right)};$$
$$\frac{\partial\sigma_{\rm eq}}{\partial\Delta\varepsilon^p_{\rm eq}} = \left[\frac{\partial\sigma_{\rm eq}}{\partial\boldsymbol{\sigma}}\right]^T \cdot \frac{\partial\boldsymbol{\sigma}}{\partial\Delta\varepsilon^p_{\rm eq}}. \tag{A.2}$$

As $\sigma_{\rm eq}$ is equal to $\sqrt{(\sigma_{11})^2 + (\sigma_{22})^2 - (\sigma_{11}\sigma_{22}) + 3(\sigma_{12})^2}$, the derivative $\partial\sigma_{\rm eq}/\partial\boldsymbol{\sigma}$ is given by the following vector form:

$$\frac{\partial\sigma_{\rm eq}}{\partial\boldsymbol{\sigma}} = \frac{1}{2\sigma_{\rm eq}}\left\{(2\sigma_{11} - \sigma_{22}), (\sigma_{11} - 2\sigma_{22}), (3\sigma_{12})\right\}^T. \tag{A.3}$$

As to the derivative $\partial\boldsymbol{\sigma}/\partial\Delta\varepsilon^p_{\rm eq}$, it can be straightforwardly obtained from Eq. (32) as follows:

$$\frac{\partial\boldsymbol{\sigma}}{\partial\Delta\varepsilon^p_{\rm eq}} = -\frac{\mathbb{C}^e \cdot \mathbb{I}_d \cdot \boldsymbol{\sigma}}{\sigma_{\rm eq}}. \tag{A.4}$$

The derivatives $\partial\Delta\varepsilon^p/\partial\Delta\varepsilon^p_{\rm eq}$, $\partial\Delta\varepsilon^p_{11}/\partial\Delta\varepsilon^p_{\rm eq}$, and $\partial\Delta\varepsilon^p_{22}/\partial\Delta\varepsilon^p_{\rm eq}$ can be determined from Eq. (31):

$$\frac{\partial\Delta\boldsymbol{\varepsilon}^p}{\partial\Delta\varepsilon^p_{\rm eq}} = \frac{\mathbb{I}_d \cdot \boldsymbol{\sigma}^{\rm Tr}}{\sigma^{\rm Tr}_{\rm eq}}; \qquad \frac{\partial\Delta\varepsilon^p_{11}}{\partial\Delta\varepsilon^p_{\rm eq}} = \frac{\left(\mathbb{I}_d \cdot \boldsymbol{\sigma}^{\rm Tr}\right)_1}{\sigma^{\rm Tr}_{\rm eq}}; \qquad \frac{\partial\Delta\varepsilon^p_{22}}{\partial\Delta\varepsilon^p_{\rm eq}} = \frac{\left(\mathbb{I}_d \cdot \boldsymbol{\sigma}^{\rm Tr}\right)_2}{\sigma^{\rm Tr}_{\rm eq}}. \tag{A.5}$$

The convergence of the Newton–Raphson iterative process is reached when $|\mathcal{J}(\Delta\varepsilon^{p(i)}_{\rm eq})|$ becomes smaller than 10^{-10}.

Appendix B. Typical Input File to Output Elementary Stiffness Matrices

The example below is an excerpt from a typical input file with the added lines shown in red. Such lines must be added to extract the global and elementary stiffness matrices. In these command lines, 'Nel' and 'n' denote the total number of elements and the record frequency of the elementary stiffness matrices, respectively.

Input file (.inp)

```
** ----------------------------------------------------------------
** ASSEMBLY
**
*Assembly, name=Assembly
**
*Elset, elset=SET-ALL, instance=Part-1-1, generate
1, Nel, 1
..........
*End Assembly
** ----------------------------------------------------------------
**
*STEP, name=ExportK1
*MATRIX GENERATE, MPC=NO, STIFFNESS
*MATRIX OUTPUT, STIFFNESS, FORMAT=COORDINATE
*END STEP
** ----------------------------------------------------------------
** STEP: Step-1
**
*Step, name=Step-1, nlgeom=YES, inc=100000
.....
*ELEMENT MATRIX OUTPUT, ELSET=SET-ALL, FREQUENCY=n, STIFF-
NESS=YES, OUTPUT FILE=USER DEFINED, FILE NAME=K_UNI_X
*End Step
```

Appendix C. Key Parts and Some Sections of the Python Script

These scripts take as input the following .mtx files generated by ABAQUS software:

- K_UNI_X.mtx: The elementary stiffness matrices of Nel elements at each increment.
- JOB_UNI_X_STIF1.mtx: The initial global stiffness of the Nel elements before loading.

Python script (.py)

```
#=========================================================================
# Read data from: K_UNI_X.mtx: Number of elements (elenum) and number
                                    of increments (incnum)
#=========================================================================
#=========================================================================
# Read data from JOB_UNI_X_STIF1.mtx to build the initial global
                                    stiffness matrix
#=========================================================================

with open('JOB_UNI_X_STIF1.mtx') as ff:
    lineKg = ff.readlines()
    ff.close
```

```
for i in range(len(lineKg)):
    lineKg[i]=lineKg[i].strip(',\n\r')
    lineKg[i]=lineKg[i].replace('  ',' ')
    lineKg[i]=lineKg[i].replace(' ',',')
    lineKg[i]=re.split(',',lineKg[i])
ddl_nbr=6
row=[]
col=[]
data=[]
i=0
for i in range (len(lineKg)):
    row.append(int(lineKg[i][0])-1)
    col.append(int(lineKg[i][1])-1)
    data.append(float(lineKg[i][2]))
print(len(data))
row = list(map(int, row))
col = list(map(int, col))
mtx = sparse.coo_matrix ((data, (row, col)), shape=(max(row)+1, max(
                                    col)+1))
mtx = mtx.todense()

#=====================================================================
# Apply the Boundary Conditions and compute the eigenvalues of the
                                    initial global stiffness matrix
#=====================================================================

ibc=np.where(mtx==np.max(data))[0]
gc.collect()
mtx = np.delete(mtx,ibc,axis=0)
mtx = np.delete(mtx,ibc,axis=1)
gc.collect()
eigenvalues, eigenvectors = sp.sparse.linalg.eigsh(np.linalg.inv(mtx),
                                     k=5, which='LM', mode='buckling')
print('eigenvalues_Elastic_STIF1= {} '.format(eigenvalues))

#=====================================================================
# Assembly of the global matrix for incnum increment and compute
                                    eigenvalues at each increment
#=====================================================================

ic=0
K_BC1=[]
lamda=np.ones((incnum,2))
icc=np.ones(incnum)
```

```
while ic<incnum:
    f=open('K_UNI_X.mtx')
    line_inc=f.readlines()[ic*92*elenum:(ic+1)*92*elenum]
    f.close()
    line3=[]
    K_BC1=[]
    line2_inc=[]
    for i in range(len(line_inc)):
        if line_inc[i].startswith('*USER ELEMENT, NODES=         4,
                                            LINEAR'):
            line2_inc.append(line[i+2])
            line3.append(line_inc[i+5:i+89])
```

```
    for i in range(len(line2_inc)):#from string to float
         line2_inc[i]=re.findall(r"\d+\.?\d*",line2_inc[i])
    for i in range(len(line3)):
        for j in range(len(line3[i])):
            line3[i][j]=line3[i][j].strip(',\n\r')
            line3[i][j]=line3[i][j].replace(' ','')
            line3[i][j]=re.split(',',line3[i][j])

#=====================================================================
# Assembly of the incremental elementary matrices: Build the
                                    incremental global stiffness matrix
                                     K_BC1
#=====================================================================
#=====================================================================
# Apply the Boundary Conditions and Compute eigenvalues of the
                                    incremental global stiffness matrix
                                     K_BC1
#=====================================================================

    K_BC1 = np.delete(K_BC1, ibc, axis=0)
    K_BC1 = np.delete(K_BC1, ibc, axis=1)
    eigenvalues, eigenvectors = sp.sparse.linalg.eigsh(np.linalg.inv(
                                        K_BC1), k=5, which='LM', mode='
                                        buckling')
    print('ic= {} : \n eigenvalues = {} '.format(ic, eigenvalues))
    lamda[ic,0]=incnum_sav[ic]
    lamda[ic,1]=eigenvalues[0]
    np.savetxt('resultats_UNIX_FT.txt', lamda, fmt='%.6f')
    ic+=1
```

ORCID

M. BelHadjAmor https://orcid.org/0000-0003-1890-617X

M. Ben Bettaieb https://orcid.org/0000-0001-9308-2807

S. Mezlini https://orcid.org/0000-0003-1209-4246

F. Abed-Meraim https://orcid.org/0000-0003-1196-7009

References

Akpama, H., Ben Bettaieb, M. and Abed-Meraim, F. [2017] "Localized necking predictions based on rate-independent self-consistent polycrystal plasticity: Bifurcation analysis versus imperfection approach," *International Journal of Plasticity* **91**, 205–237.

Bathe, K. [2014] *Finite Element Procedures*, second edn. (Klaus-Jürgen Bathe).

Ben Bettaieb, M. and Abed-Meraim, F. [2015] "Investigation of localized necking in substrate-supported metal layers: Comparison of bifurcation and imperfection analyses," *International Journal of Plasticity* **65**, 168–190.

Ben Bettaieb, M. and Abed-Meraim, F. [2017a] "Effect of kinematic hardening on localized necking in substrate-supported metal layers," *International Journal of Mechanical Sciences* **123**, 177–197.

Ben Bettaieb, M. and Abed-Meraim, F. [2017b] "Localized necking in elastomer-supported metal layers: Impact of kinematic hardening," *Journal of Applied Mechanics, Transactions ASME* **139**(6).

Ben Bettaieb, M. and Abed-Meraim, F. [2021] "Formability prediction of substrate-supported metal layers using a non-associated plastic flow rule," *Journal of Materials Processing Technology* **287**, 116694.

Ben Bettaieb, M., Lemoine, X., Duchêne, L. and Marie Habraken, A. [2011] "On the numerical integration of an advanced Gurson model," *International Journal for Numerical Methods in Engineering* **85**, 1049–1072.

Bleich, F. [1952] *Buckling Strength of Metal Structures* (McGraw-Hill, New York).

Cicala, P. [1950] "On plastic buckling of a compressed strip," *Journal of Aerosol Science* **17**(6), 378.

Combescure, A. and Jullien, J.-F. [2015] "ASTER Shell: A simple concept to significantly increase the plastic buckling strength of short cylinders subjected to combined external pressure and axial compression," *Advanced Modeling and Simulation in Engineering Sciences* **2**(1), 2–26.

Do, V. D., Le Grognec, P. and Rohart, P. [2023] "Closed-form solutions for the elastic-plastic buckling design of shell structures under external pressure," *European Journal of Mechanics - A/Solids* **98**, 104861.

Guarracino, F. and Simonelli, M. G. [2017] "The torsional instability of a cruciform column in the plastic range: Analysis of an old conundrum," *Thin-Walled Structures* **113**, 273–286.

Hill, R. [1958] "General theory of uniqueness and stability in elastic-plastic solids," *Journal of the Mechanics and Physics of Solids* (6), 236–249.

Hopperstad, O. S., Langseth, M. and Tryland, T. [1999] "Ultimate strength of aluminium alloy outstands in compression: Experiments and simplified analysis," *Thin-Walled Structures* **34**(4), 279–294.

Hughes, T. J. and Winget, J. [1980] "Finite rotation effects in numerical integration of rate constitutive equations arising in large-deformation analysis," *International Journal for Numerical Methods in Engineering* **15**(12), 1862–1867.

Hutchinson, J. and Budiansky, B. [1976] "Analytical and numerical study of the effects of initial imperfections on the inelastic buckling of a cruciform column," in *Proceedings of the IUTAM Symposium on Buckling of Structures* (Springer, Berlin), pp. 98–105.

Hutchinson, J. W. [1970] "Elastic-plastic behaviour of polycrystalline metals and composites," *Proceedings of the Royal Society A* **319**, 247–272, doi: 10.1098/rspa.1970.0177.

Hutchinson, J. W. [1972] "On the postbuckling behavior of imperfection-sensitive structures in the plastic range," *Journal of Applied Mechanics, Transactions ASME* **39**(1), 155–162.

Jacquet, N., Tardif, N., Elguedj, T. and Garnier, C. [2022] "Buckling of thick elasto-viscoplastic egg shells under external pressure: Experiments and bifurcation analysis," *International Journal of Solids and Structures* **257**, 111591.

Jedidi, M. Y., Ben Bettaieb, M., Abed-Meraim, F., Khabou, M. T., Bouguecha, A. and Haddar, M. [2020] "Prediction of necking in HCP sheet metals using a two-surface plasticity model," *International Journal of Plasticity* **128**, 102641.

Legendre, J., Le Grognec, P., Doudard, C. and Moyne, S. [2019] "Analytical, numerical and experimental study of the plastic buckling behavior of thick cylindrical tubes under axial compression," *International Journal of Mechanical Sciences* **156**, 494–505.

Lubliner, J. [2008] *Plasticity Theory* (Dover Publications).

Nasikas, A., Karamanos, S. A. and Papanicolopulos, S. A. [2022] "A framework for formulating and implementing non-associative plasticity models for shell buckling computations," *International Journal of Solids and Structures* **257**, 111508.

Nguyen, K., Sanz, M. A. and Montáns, F. J. [2020] "Plane-stress constrained multiplicative hyperelasto-plasticity with non-linear kinematic hardening. Consistent theory based on elastic corrector rates and algorithmic implementation," *International Journal of Plasticity* **128**.

Nguyen, Q. S. [2000] *Stability and Non-linear Solid Mechanics* (Wiley).

Ning, X. and Pellegrino, S. [2017] "Experiments on imperfection insensitive axially loaded cylindrical shells," *International Journal of Solids and Structures* **115–116**, 73–86.

Onat, E. and Drucker, D. [1953] "Inelastic instability and incremental theories of plasticity," *Journal of Aerosol Science* **20**(3), 181–186.

Paux, J., Ben Bettaieb, M., Badreddine, H., Abed-Meraim, F., Labergere, C. and Saanouni, K. [2020] "An elasto-plastic self-consistent model for damaged polycrystalline materials: Theoretical formulation and numerical implementation," *Computer Methods in Applied Mechanics and Engineering* **368**, 113138.

Ramberg, W. and Osgood, W. R. [1943] "Description of stress-strain curves by three parameters," Tech. rep.

Reinssner, E. [1945] "The effect of transverse shear deformation on the bending of elastic plates," *Journal of Applied Mechanics* **12**(2), 69–77.

Ruocco, E. [2015] "Elastic/plastic buckling of moderately thick plates and members," *Computers and Structures* **158**, 148–166.

Sewell, M. J. [1973] "A yield-surface corner lowers the buckling stress of an elastic-plastic plate under compression," *Journal of the Mechanics and Physics of Solids* **21**(1), 19–45, doi: 10.1016/0022-5096(73)90028-8.

Sewell, M. J. [1974] "A plastic flow rule at a yield vertex," *Journal of the Mechanics and Physics of Solids* **22**(6), 469–490, doi: 10.1016/0022-5096(74)90029-5.

Shamass, R., Alfano, G. and Guarracino, F. [2014] "A numerical investigation into the plastic buckling paradox for circular cylindrical shells under axial compression," *Engineering Structures* **75**, 429–447.

Shamass, R., Alfano, G. and Guarracino, F. [2017] "On elastoplastic buckling analysis of cylinders under non-proportional loading by differential quadrature method," *International Journal of Structural Stability and Dynamics* **17**(7), 1750072.

Shanley, F. R. [1947] "Inelastic column theory," *Journal of the Aeronautical Sciences* **14**(5), 261–268.

Smith, S. T., Bradford, M. A. and Oehlers, D. J. [2003] "Inelastic buckling of rectangular steel plates using a Rayleigh-Ritz method," *International Journal of Structural Stability and Dynamics* **03**(04), 503–521.

Timoshenko, S. and Gere, J. M. [1961] *Theory of Elastic Stability* (McGraw-Hill).

Wagner, H. N., Sosa, E. M., Ludwig, T., Croll, J. G. and Hühne, C. [2019] "Robust design of imperfection sensitive thin-walled shells under axial compression, bending or external pressure," *International Journal of Mechanical Sciences* **156**, 205–220.

Wang, C. M. [1995] "Allowance for prebuckling deformations in buckling load relationship between Mindlin and Kirchhoff simply supported plates of general polygonal shape," *Engineering Structures* **17**(6), 413–418.

Wang, C. M. [2004] "Plastic buckling of simply supported, polygonal mindlin plates," *Journal of Engineering Mechanics* **130**(1), 117–122.

Wang, C. M. and Aung, T. M. [2007] "Plastic buckling analysis of thick plates using p-Ritz method," *International Journal of Solids and Structures* **44**(18–19), 6239–6255.

Wang, C. M., Xiang, Y. and Chakrabarty, J. [2001] "Elastic/plastic bucking of thick plates," *International Journal of Solids and Structures* **38**, 8617–8640.

Wang, X. and Huang, J. C. [2009] "Elastoplastic buckling analyses of rectangular plates under biaxial loadings by the differential qudrature method," *Thin-Walled Structures* **47**(1), 14–20.

Zhang, W. and Wang, X. [2011] "Elastoplastic buckling analysis of thick rectangular plates by using the differential quadrature method," *Computers and Mathematics with Applications* **61**(1), 44–61.

Zhu, J., Ben Bettaieb, M. and Abed-Meraim, F. [2022] "Comparative study of three techniques for the computation of the macroscopic tangent moduli by periodic homogenization scheme," *Engineering with Computers* **368**, 113138.

Zhu, J. C., Ben Bettaieb, M., Zhou, S. and Abed-Meraim, F. [2023] "Ductility limit prediction for polycrystalline aggregates using a CPFEM-based multiscale framework," *International Journal of Plasticity* **167**, 103671.